Journal of Nanobiotechnology

RESEARCH

Open Access

S-RBD-modified and miR-486-5p-engineered exosomes derived from mesenchymal stem cells suppress ferroptosis and alleviate radiation-induced lung injury and long-term pulmonary fibrosis

Wei-Yuan Zhang[1,2], Li Wen[3], Li Du[4], Ting Ting Liu[5], Yang Sun[1,2], Yi-Zhu Chen[4], Yu-Xin Lu[4], Xiao-Chen Cheng[4], Hui-Yan Sun[6], Feng-Jun Xiao[4*] and Li-Sheng Wang[1,2,3*]

Abstract

Background Radiation-induced lung injury (RILI) is associated with alveolar epithelial cell death and secondary fibrosis in injured lung. Mesenchymal stem cell (MSC)-derived exosomes have regenerative effect against lung injury and the potential to intervene of RILI. However, their intervention efficacy is limited because they lack lung targeting characters and do not carry sufficient specific effectors. SARS-CoV-2 spike glycoprotein (SARS-CoV-2-S-RBD) binds angiotensin-converting enzyme 2 (ACE2) receptor and mediates interaction with host cells. MiR-486-5p is a multifunctional miRNA with angiogenic and antifibrotic potential and acts as an effector in MSC-derived exosomes. Ferroptosis is a form of cell death associated with radiation injury, its roles and mechanisms in RILI remain unclear. In this study, we developed an engineered MSC-derived exosomes with SARS-CoV-2-S-RBD- and miR-486-5p- modification and investigated their intervention effects on RIPF and action mechanisms via suppression of epithelial cell ferroptosis.

Results Adenovirus-mediated gene modification led to miR-486-5p overexpression in human umbilical cord MSC exosomes ($p < 0.05$), thereby constructing miR-486-5p engineered MSC exosomes (miR-486-MSC-Exo). MiR-486-MSC-Exo promoted the proliferation and migration of irradiated mouse lung epithelial (MLE-12) cells in vitro and inhibited RILI in vivo (all $p < 0.05$). MiR-486-MSC-Exo suppressed ferroptosis in MLE-12 cells, and an in vitro assay revealed that the expression of fibrosis-related genes is up-regulated following ferroptosis (both $p < 0.05$). MiR-486-MSC-Exo reversed the up-regulated expression of fibrosis-related genes induced by TGF-β1 in vitro and improved pathological fibrosis in RIPF mice in vivo (all $p < 0.05$). SARS-CoV-2-S-RBD-modified and miR-486-5p-engineered MSC exosomes (miR-486-RBD-MSC-Exo) were also constructed, and the distribution of DiR dye-labeled miR-486-RBD-MSC-Exo in $hACE2^{CKI/CKI}$ Sftpc-Cre^{+} mice demonstrated long-term retention in the lung ($p < 0.05$). MiR-486-RBD-MSC-Exo significantly improved the survival rate and pathological changes in $hACE2^{CKI/CKI}$ Sftpc-Cre^{+} RIPF mice (all $p < 0.05$).

*Correspondence:
Feng-Jun Xiao
xiaofjun@sina.com
Li-Sheng Wang
lishengwang@qdu.edu.cn
Full list of author information is available at the end of the article

Furthermore, miR-486-MSC-Exo exerted anti-fibrotic effects via targeted SMAD2 inhibition and Akt phosphorylation activation ($p < 0.05$).

Conclusions Engineered MSC exosomes with SARS-CoV-2-S-RBD- and miR-486-5p-modification were developed. MiR-486-RBD-MSC-Exo suppressed ferroptosis and fibrosis of MLE-12 cells in vitro, and alleviated RILI and long-term RIPF in ACE2 humanized mice in vivo. MiR-486-MSC-Exo exerted anti-fibrotic effects via SMAD2 inhibition and Akt activation. This study provides a potential approach for RIPF intervention.

Keywords Mesenchymal stem cells, Engineered exosomes, SARS-CoV-2-S-RBD, MiR-486-5p, Ferroptosis, Radiation-induced pulmonary injury, Pulmonary fibrosis

Graphical Abstract

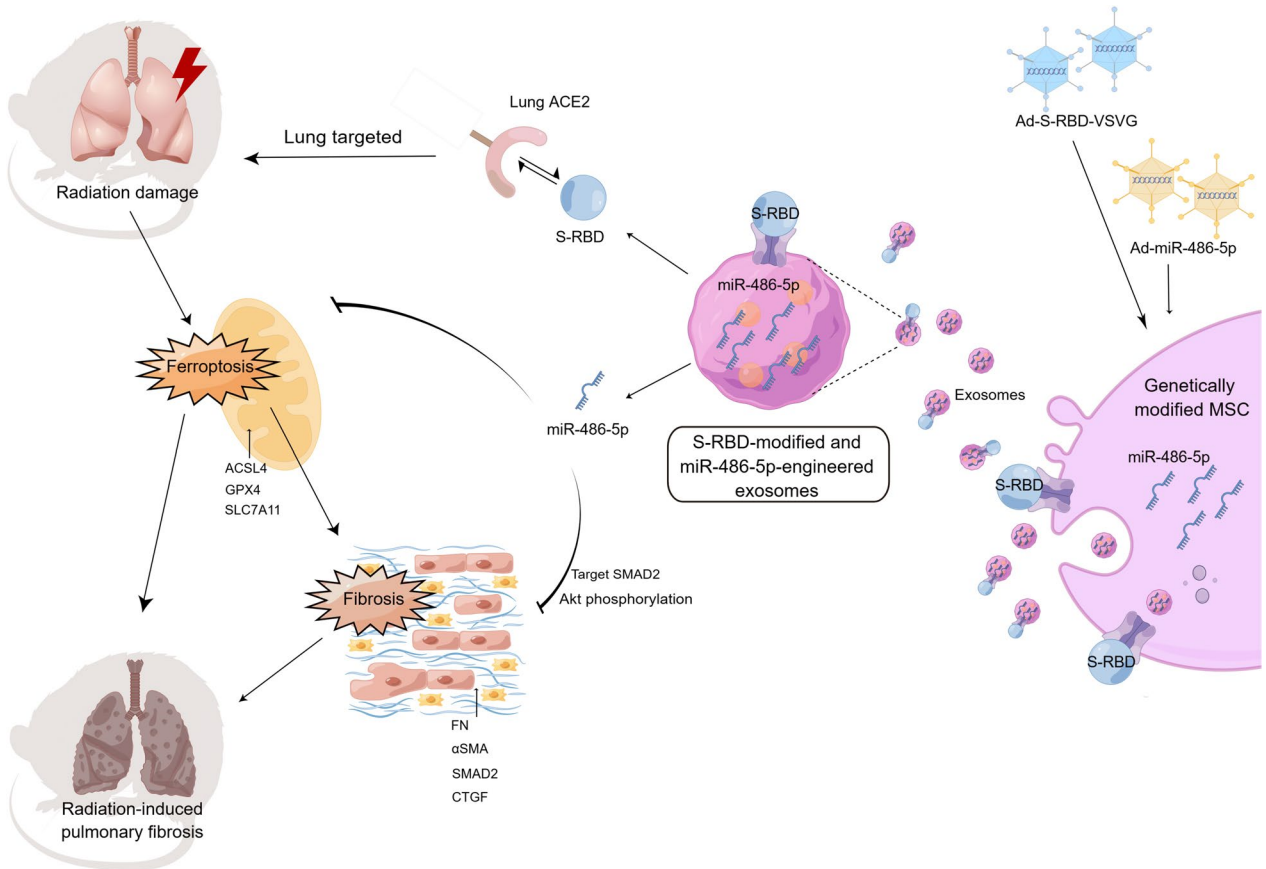

Background

Thoracic radiotherapy is a major treatment modality for thoracic tumors. However, thoracic radiotherapy also has a secondary effect on normal lung tissues. Radiation-induced lung injury (RILI) occurs in 5–20% of patients and limits the maximum dose of radiotherapy [1]. RILI manifests acutely as radiation pneumonitis and chronically as radiation-induced lung fibrosis (RIPF) [2]. Currently, there remains a lack of effective interventions for the treatment of lung fibrosis, known strategies include early intervention of RILI. Mesenchymal stem cells (MSCs) are multipotent stromal cells capable of differentiating into cell types of mesodermal origin. Multiple advances have been reported regarding their clinical trials of various conditions, including orthopedic injuries, graft versus host disease following bone marrow transplantation, cardiovascular diseases, autoimmune diseases, and liver diseases [3]. MSCs are being also explored in the treatment of lung tissue injury and fibrosis [4, 5].

Potential therapies on the application of MSCs in RIPF remain at the preclinical stage.

Exosomes are extracellular vesicles (EVs) that contain multiple bioactive substances such as lipid membranes, mRNAs, miRNAs and proteins [6, 7]. Recent investigations revealed exosomes reflect biophysical features of MSCs and are considered more effective than MSCs themselves [8]. MSC-derived exosomes are smaller and less immunogenic than MSCs and can effectively deliver bioactive molecules to effector organs, possessing stable storage and controlled release characteristics [9, 10]. MSC exosomes carrying regenerative factors have become an promising therapeutic strategy for RIPF [11]. Distribution studies have shown that MSCs primarily accumulate in the lungs following systemic administration. In vivo distribution characteristics of MSC-derived exosomes differ from those of MSCs. New approaches based on the interactions of biomolecules can enable retargeted distribution of MSC-derived exosomes to organs [12, 13].

Angiotensin converting enzyme 2 (ACE2) is a type I transmembrane protein and serves as a receptor of severe acute respiratory syndrome coronavirus-2 (SARS-CoV-2) [14]. The SARS-CoV-2 spike glycoprotein binds to the host cell ACE2 receptor through its receptor binding domain (SARS-CoV-2-S-RBD) and mediates viral infection [14]. Crystal structure analysis of the human ACE2 (hACE2) receptor complex has identified the binding sites of hACE2 and SARS-CoV-2-S-RBD. Based on the interaction between SARS-CoV-2-S-RBD and hACE2, it is possible to achieve the targeting of $ACE2^{+}$ cells to receive RBD-loaded MSC exosomes. Single-cell sequencing data revealed that ACE2 is mainly expressed in type II alveolar, vascular endothelial, and interstitial cells, all of which are sensitive to radiation damage [15]. ACE2 is also an inflammation response gene and upregulated in the injured lung [16]. Thus, SARS-CoV-2-S-RBD mediated ACE2 binding may retarget exosomes to ACE2 high expressed tissues, especially injured lung.

Exosomal miRNAs can regulate immunity, inhibit inflammation, and promote epithelial tissue repair in injured lung tissues [17]. Targeted delivery of miRNAs with anti-fibrotic effects through exosomes may enhance their efficacy of RIPF treatment. MiR-486-5p was first found in a human fetal liver cDNA library and was identified as a regulator of leukemia [18, 19]. As a multifunctional miRNA, miR-486-5p exhibits angiogenic and anti-fibrotic activities in liver injury and hepatic fibrosis [20]. MiR-486-5p expression is decreased in serum and lung tissues of patients with silicosis and idiopathic pulmonary fibrosis [21]. Growing evidence indicated that miR-486-5p has the potential to regulate inflammation and fibrosis in lung tissue [21–23]. However, whether miR-486-5p reduces radiation-induced damage by suppressing inflammation and cell death in the early stages of RIPF remains unclear.

Ferroptosis is a type of cell death associated with iron accumulation, lipid peroxidation and ROS production [24]. Emerging evidence has suggested that ferroptosis is associated with the pathogenesis of fibrosis [25, 26]. Ferroptosis triggers an inflammatory response, promotes epithelial-mesenchymal transition, and ultimately leads to fibrosis [26]. And several reports mentioned therapeutic potential of ferroptosis inhibitors and iron chelators in treating fibrosis [27]. Erastin is a widely used ferroptosis inducer in research and considered to induce typical iron-dependent cell death. MSC-derived exosomes have inhibitory effects on ferroptosis in various cell types. Based on the activity of MSC-derived exosomes and their susceptibility to modification of miRNAs, engineered MSC-derived exosomes carrying miR-486-5p might enhance its efficacy in interfering erastin-induced alveolar epithelial cell ferroptosis and preventing RIPF. In this study, we developed a surface RBD-loaded MSC-derived exosome for the targeted delivery of miR-486-5p and investigated its role in the early interference of RILI and late prevention of RIPF.

Methods

Cell lines and human umbilical cord mesenchymal stem cells (UC-MSCs)

Mouse lung epithelial cells (MLE-12) were purchased from Procell Biologics and cultured in DMEM / F12 medium (11,330,032, Gibco) supplemented with 2% fetal bovine serum (FBS; 10099141C, Gibco) and 0.01 mg/ mL transferrin (T8010, Solarbio). Primary human UC-MSCs were obtained from Allcare Biotechnology Co., Ltd. and cultured in serum-free medium (1001A; Clin-Biotech).

Isolation and characterization of exosomes

The 72 h-supernatant from cell cultures of MSCs (or engineered MSCs in later experiments) was harvested, centrifuged at 300 g for 10 min to remove cellular debris, and subsequently centrifuged at 2000 g for 10 min to remove microvesicles. Then, the exosomes were pelleted using ultracentrifugation at 120,000 g, 4 °C for 90 min (Beckman Coulter, Inc., USA), washed with 20 mL of 1 × PBS and ultracentrifuged again at 120,000 g, 4 °C for 90 min. The exosome-enriched pellets were collected and suspended in 1 × PBS for use. Morphological analysis of the exosomes was performed using transmission electron microscopy (TEM) (Hitachi, Japan). Nanoparticle tracking Analysis (NTA) is a laser scattering and tracking technique that can track, measure and analyze the size distribution and concentration of nanoparticles in liquids in real time and with high resolution. The particle

size, number and distribution of exosomes were determined using NTA (Zetaview, Particle Metrix). CD63 is a major membrane protein of exosomes, involved in exosome biogenesis and release. CD81 is another important protein of exosome membranes, involved in interactions between exosomes and target cells. Heat shock protein 70 (HSP70) plays a crucial role in exosome biogenesis and protein loading. Tumor susceptibility gene 101 (TSG101) is a key factor in exosome biogenesis and sorting mechanisms, involved in exosome formation and release. The expression of exosomal surface markers, including CD63, CD81, HSP70 and TSG101, was detected by western blotting using antibodies from Proteintech. Glyceraldehyde 3-phosphate dehydrogenase (GAPDH; Cell Signaling Technology) was used as an internal control.

Exosome sequencing

MSC-derived exosomes (1×10^8) were resuspended in 1×PBS and then sent to Applied Protein Tech. Bio. for small RNA sequencing. Specifically, total exosomal RNA was extracted for parallel quality testing and a small RNA library was constructed using Illumina's TruSeq small RNA sample prep kit. The library was purified, inspected, and quantified using polymerase chain reaction (PCR) amplification by connecting the sequencing joint and index. Sequencing was performed using the Illumina platform. The data were de-jointed and quality filtered, and the filtered sequences used for deduplication processing. The identical sequences were merged, and the corresponding abundance of each sequence was recorded. The deduplicated small RNA sequences were annotated based on the reference genome, and the abundance of the corresponding annotation was given. The sequences of precursor and mature human miRNAs were downloaded from miRBase and compared to the de-duplicated sequences, so as to annotate the detected miRNAs. To effectively utilize resources and understand biological functions, the top 30 expressed miRNAs with significance were selected from the sequencing results for subsequent analysis.

Adenovirus production and cell transfection

The PHBAd-U6-GFP-mmu-miR486-5p recombinant vector has been described previously [28]. The recombinant adenovirus vector miR-486-5p overexpression plasmid and the skeleton plasmid pHBAd BHG were transfected into HEK293 cells using Lipofiter™ transfection reagent. The virus supernatant was collected and amplified, concentrated with CsCl combined with ultracentrifugation, and stored at—80 ℃ until use. The PHBAd-U6-GFP-Scramble vector was used as a control. The vector titer was determined by infecting HEK293 cells and analyzing the expression of green fluorescent protein. MSCs were infected with recombinant adenoviruses according to the ratio of virus number to cell number, i.e., multiplicity of infection (MOI) = 0, 25, 50, 100, 150 and 200. After 8 h, the medium was replaced with complete medium. After 48 h, the expression of green fluorescent protein (GFP) in MSC was evaluated by fluorescence microscopy and cell samples were collected measurement of miR-486-5p expression using reverse transcription real-time quantitative polymerase chain reaction (RT-qPCR). Based on the study of Fu and colleagues [29], we used the GV343-CV140-GFP-RBD-VSVG viral vector, which was provided by Genechem Bio.. UC-MSCs were infected with the constructed adenoviruses to obtain miR-486-5p engineered MSC (miR-486-MSC) and RBD-VSVG-engineered MSC (RBD-MSC). According to the fluorescence level and the target molecular expression level, MOI = 150 was selected for subsequent experiments.

Establishment and treatment of irradiated cell models

MLE-12 cells were cultured and seeded in plates until they grew to about 60% confluence. MLE-12 cells were irradiated with a single dose of 10 Gy γ-rays at room temperature. The radiation dose was based on previous literature and adjusted appropriately according to the cell growth [30, 31]. Immediately after irradiation, MSC-derived exosomes (MSC-Exo) and miR-486-5p engineered MSC exosomes (miR-486-MSC-Exo) were directly added to each well (50 μg/mL), and 1×PBS was used as the control. After incubation at 37 °C in 5% CO_2 for 24, 48, 72, or 96 h, samples were collected for proliferation, morphometry and migration assays.

Establishment and treatment of ferroptosis cell models

MLE-12 cells were cultured and seeded in plates. When the MLE-12 cells grew to approximately 60% confluence, erastin (S7242, Selleck) was added to each well to achieve a final concentration of 0, 0.5, 1, 2, 4, 8 μM. Immediately after erastin addition, MSC-Exo and miR-486-MSC-Exo were directly added to each well (50 μg/mL), and 1×PBS was used as the control. A ferroptosis inhibitor (Ferrostatin-1; Fer-1) was used as the positive control. After 24 or 48 h of incubation in 5% CO_2 at 37 °C, cells were collected for viability, morphometry and mRNA assays.

When MLE-12 cells reached approximately 60% confluence, erastin was added to each well (final concentration 1 μM). After 12 h of erastin treatment, the cell culture supernatant was replaced with complete medium. After an additional 24 h, the cell culture supernatant was transferred to another set of MLE-12 cells at 60%, followed immediately by the addition of MSC-Exo and miR-486-MSC-Exo to each well (concentration 50 μg/mL), with 1×PBS used as a control. Subsequently, cells were

incubated at 37 °C, 5% CO_2 for 24, 48, or 72 h before collecting cellular mRNA for qPCR analysis.

Establishment and treatment of fibrotic cell models

MLE-12 cells were cultured and seeded onto well plates, and TGF-β1 (CK33, Novoprotein) was added to each well to achieve a final concentration of 0, 1, 2, 4 ng/mL. Immediately after TGF-β1 added, MSC-Exo and miR-486-MSC-Exo were directly added to each well (50 μg/mL), and 1 × PBS was used as the control. Cells were collected for gene expression analysis after incubation in 5% CO_2 at 37 °C for 24 or 48 h.

Cell-counting-kit-8 (CCK-8) proliferation assay

MLE-12 cells were cultured in DMEM / F12 medium supplemented with 2% FBS and 0.01 mg/ mL transferrin and were seeded into 96-well plates at 8000 cells per well in a 100 μL culture system. After irradiation for 0, 24, 48, 72, and 96 h or erastin treatment for 0, and 24 h, 10 μL CCK-8 solution (B34304, Bimake) was added to each well. The culture plates were incubated for 3 h, during which the CCK-8 dye was reduced to yellow by dehydrogenase in the cells, the reaction signal was detected using a microplate reader.

Morphological assessment

After irradiation for 48 h or erastin treatment for 24 h, MLE-12 cells were fixed with 4% paraformaldehyde (PFA), stained using a Giemsa staining kit (G1015, Solarbio) according to the manufacturer's instructions, and observed under a light microscope.

Divalent iron detection

After erastin treatment for 24 h, MLE-12 cells were fixed with 4% PFA. A Lillie divalent iron staining kit (G3320, Solarbio) was used to stain the cells at room temperature for 30 min. In the assay, Fe^{3+} inside the cells is reduced to Fe^{2+} via the Prussian blue reaction, which subsequently turns blue upon treatment with potassium ferrocyanide and dilute acid. This allowed microscopic observation of the distribution and deposition of iron within the cells.

Cell scratch assay

Irradiated or non-irradiated MLE-12 cells were grown in 6-well plates until confluence, and mechanical damage was induced by scratching the confluent cell monolayer with a sterile pipette tip. Injured MLE-12 monolayers were washed three times with 1 × PBS to remove cell debris, and then incubated with exosomes (30 μg/mL) or 1 × PBS for 24 h. Cell migration was assessed by measuring the mean healing ratio of the scratched area. A picture was taken with a microscope (Olympus, Tokyo, Japan) upon initiation of the scratch (0 h), and the scratched edges of cells were marked with image analysis software (Photoshop 2020) to calculate the average scratched distance and area. The healing of the scratch was then measured as the percentage scratch area at 6, 12, and 24 h time points in relation to the original scratch area (= 100%).

Dihydroethidium staining

The MLE-12 cells were seeded onto confocal slides and divided into control, erastin + 1 × PBS, erastin + MSC-Exo, erastin + miR-486-MSC-Exo, and erastin + Fer-1 group. Erastin was added to the corresponding groups, at the same time as 1 × PBS, MSC-Exo, miR-486-MSC-Exo or Fer-1 (control). After 24 h, the supernatant was aspirated and discarded. Dihydroethidium (DHE) staining solution (S0063, Beyotime) was added and the cells incubated at 37 °C for 20 min in the dark, followed by addition of 4% PFA for 30 min. The slides were then removed from the fixative, rinsed repeatedly with 1 × PBS, and sealed with a DAPI containing tablet.

Table 1 Primer sequences used in reverse transcription real-time quantitative polymerase chain reaction

	Forward	Reverse
miR-486-5p	5′- TCCTGTACTGAGCTGCCCCGAG-3′	5′- GATTGAATCGAGCACCAGTTAC-3′
U6	5′- CGCTTCGGCAGCACATATACTA-3′	5′- GATTGAATCGAGCACCAGTTAC-3′
GPX4	5′-GATGGAGCCCATTCCTGAACC-3′	5′-CCCTGTACTTATCCAGGCAGA-3′
ACSL4	5′-GGCACCGTCATCGGATCAG-3′	5′-CTCCACAGGCAGACCAGAAAA-3′
SLC7A11	5′-CTCACCATTATATTGCTGCCTGT-3	5′-TCTCTTTGCCATAGCGTTTTTCT-3′
FN	5′-TCTGGGAAATGGAAAAGGGGAATGG-3′	5′-CACTGAAGCAGGTTTCCTCGGTTGT3′
αSMA	5′-GACGCTGAAGTATCCGATAGAACACG-3′	5′-CACCATCTCCAGAGTCCAGCACAAT-3
SMAD2	5′-AAGCCATCACCACTCAGAATTG-3′	5′-CACTGATCTACCGTATTTGCTGT-3′
CTGF	5′-GCGAAGCTGACCTGGAGGA-3′	5′-CGCACGAGTGGTGGTTCTGTGCG-3′
GAPDH	5′-CGACTTCAACAGCAACTCCCACTCTTCC-3′	5′-TGGGTGGTCCAGGGTTTCTTACTCCTT-3′

DHE is reduced to a fluorescent compound (2',7'-dihydroxyfluorescein) inside cells under oxidative stress, thereby generating a fluorescent signal in the cells. Fluorescence was observed under a confocal microscope. ImageJ software was used to quantify the mean pixel intensity in the red channel, which equates to the ratio of red fluorescence intensity per unit field of view to the cell area, to evaluate the fluorescence signal per unit area.

Mito-tracker staining

The MLE-12 cells were seeded onto confocal slides and divided into control, erastin + 1 × PBS, erastin + MSC-Exo, erastin + miR-486-MSC-Exo, and erastin + Fer-1 group. Erastin was added to the corresponding groups, at the same time as 1 × PBS, MSC-Exo, miR-486-MSC-Exo or Fer-1. After 24 h, the supernatant was aspirated, mito-tracker staining solution (C1048, Beyotime) was added to the cells, which were incubated at 37 °C for 15 min in the dark, followed by addition of 4% PFA for 30 min. The slides were removed out, rinsed repeatedly with 1 × PBS, and sealed with a DAPI containing tablet. Mito-tracker staining uses fluorescent dyes that accumulate in regions of high mitochondrial membrane potential to visualize and analyze the position and morphology of mitochondria within cells. Green-stained mitochondria could be observed under confocal microscopy. ImageJ software was used to quantify the mean pixel intensity in the green channel, which equates to the ratio of green fluorescence intensity per unit field of view to the cell area, to evaluate the fluorescence signal per unit area.

RNA extraction and RT-qPCR

Total RNA was extracted from the cells using TRIzol reagent (Invitrogen). Each sample contained 1×10^6 cells. After RNA concentration and quality detection, cDNA was synthesized using a reverse transcription kit (AT311, TransGen) with each system containing 1 μg RNA. RT-qPCR was performed using a SYBR Green RT-qPCR kit (AQ601, TransGen) with the RT-qPCR program set as 94 °C for 30 s, 94 °C for 5 s, 60 °C for 15 s, and 72 °C for 10 s (×40 cycles). After the program was run, the time required for reading the fluorescence value of each hole to reach the plateau period was the CT value. GAPDH was used as an internal control[32], and the $2^{\triangle\triangle CT}$ values of GPX4, ACSL4, SLC7A11, FN, αSMA, SMAD2, and CTGF were calculated as relative mRNA expression levels. The primer sequences are listed in Table 1. Total miRNA was extracted from cells or exosomes using the miRcute miRNA Isolation Kit (DP501, Tiangen). Each sample contained 1×10^6 cells or 1×10^8 exosomes. The $2^{-\triangle\triangle CT}$ value of miR-486-5p was calculated as the relative expression level using the TaqMan MicroRNA Reverse Transcription Kit and TaqMan MicroRNA Assay Kit (Life Technologies, Carlsbad, CA, USA), with U6 as an internal control[33]. RT-qPCR was performed using a fluorescent quantitative PCR apparatus (QuantStudio 3; Applied Biosystems, Foster City, CA, USA).

Western blot

Cells (1×10^6) and exosomes (1×10^8) were lysed in RIPA buffer (R0010, Solarbio) containing 1% phenylmethylsulphonyl fluoride (PMSF, P0100, Solarbio). Protein concentration was determined using a BCA protein assay kit (PC0020, Solarbio). Proteins were loaded onto 10% SDS polyacrylamide gels, transferred to polyvinylidene fluoride (PVDF) membranes, and labeled with primary antibodies (rabbit anti-CD9, CD63, CD81, HSP70, TSG101 (Proteintech), FN, SMAD2, αSMA, CTGF, pAkt, Akt, GAPDH (Cell Signaling), hACE2, β-actin (abclonal) and RBD (Sinobio.)). CD9, CD63, CD81, HSP70 and TSG101 are surface marker proteins of exosomes. FN, SMAD2, αSMA, and CTGF represent fibronectin, SMAD family protein 2, alpha skeletal muscle actin and connective tissue growth factor, respectively, which are fibrosis related markers. pAkt and Akt are key molecules in the Akt signaling pathway. Subsequently, the immunoreactive bands were incubated with goat-anti-rabbit horseradish peroxidase-conjugated secondary antibodies and visualized using an enhanced chemiluminescence solution (34,096, Thermo Fisher Scientific). Protein levels were analyzed using the Scion image software (GenScript, USA).

Establishment and treatment of mouse models with RILI

Eight-week-old female C57BL/6 mice (approximately 18 g) purchased from SIPEIFU Biotechnology Co., Ltd. were acclimated for one week under standard laboratory conditions to familiarize them with the environment and reduce their stress. The mice were randomly divided into four groups: control (Con), irradiation + 1 × PBS (IR + PBS), irradiation + MSC-exosomes (IR + MSC-Exo), and irradiation + miR-486-MSC-exosomes (IR + miR-486-MSC-Exo), with 32 mice in each group. Except for the Con group, mice were anesthetized with 1% sodium pentobarbital and immobilized on an operating platform to expose their whole chest to a single dose of 20 Gy of γ-rays. The irradiation protocol was referenced from a previous study[34]. Mice in the IR + MSC-Exo and IR + miR-486-MSC-Exo groups received an intravenous dose of exosomes (200 μg per mouse in 300 μL of 1 × PBS) 6 h after irradiation and then three more times (four times in total) over the following two weeks (on days 7, 10, and 14). The injection protocol was referenced from previous studies [35]. Mice in the IR + PBS group were injected with the same volume of 1 × PBS. Mice were euthanized by cervical dislocation at 1 week,

2 weeks, 1 month, 3 months and 6 months post-injection to collect lung samples for further experiments. Efforts were made to minimize harm to the animals. All animal experiments were approved by the Laboratory Animal Centre of the Academy of Military Medical Sciences (Animal Ethics Number: IACUC-DWZX-2022–876).

Establishment of hACE2$^{CKI/CKI}$ Sftpc-Cre^{+} mice models

In the human ACE2 conditional knock-in (CKI) mouse model, the "CAG promoter-loxP-PGK-Neo-6*SV40 pA-loxP-Kozak-Human ACE2 CDS-rBG pA" cassette was inserted into ROSA26 intron 1. Homology arms for the targeting vector was generated via PCR using a BAC clone template. Cas9 and gRNA were co-injected with the targeting vector into fertilized eggs to produce KI mice. Offspring were genotyped using PCR and sequenced for analysis. This work was performed by Cyagen Biotechnology Co., Ltd.. The target mouse population was expanded by hybridization with wild-type mice and confirmed by hybridization of the offspring with alveolar epithelial-specific Cre^{+} mice (Sftpc-Cre^{+} mice) to obtain hACE2$^{CKI/CKI}$-SftpcCre^{+} mice. All animal experiments were conducted in accordance with procedures approved by the Animal Ethics Committee of the Academy of Military Medicine (IACUC-DWZX- 2022 -876).

Detection of bronchoalveolar lavage fluid

After irradiation for 0, 7, 14, and 28 d, 4 mice in each group were euthanized by cervical dislocation and the trachea-lungs were removed with sterile surgical instruments, taking care not to puncture the lung tissue. A lavage needle was inserted into the trachea and 1 mL of sterile 1 × PBS was infused. The bronchoalveolar lavage fluid (BALF) was extracted and transferred to a tube containing EDTA. After centrifugation at 12,000 × g for 15 min, the supernatant was taken and stored at -80℃. The expression levels of IL-6, TNF-α and IL-18 in BALF were detected using ELISA kits (Laizee).

Histology and hematoxylin–eosin and Masson staining

After irradiation or control treatment for 1 m, 3 m, and 6 m, 4 mice from each group were euthanized using cervical dislocation and the lungs were removed with sterile surgical instruments. Lung tissues from each mouse was fixed in 4% PFA for at least 48 h, dehydrated in a gradient of ethanol, and embedded in paraffin. The specimens were cut into 4 μm sections for hematoxylin–eosin (H&E; G8220, Solarbio) and Masson staining (G1340, Solarbio). The sections were observed and photographed under a light microscope.

The results of H&E and Masson staining of mouse lung tissue were analyzed using CaseViewer2.4 scanning and browsing software involving selection of three random areas of lung tissue sections at 200-fold imaging. Subsequently, Image-Pro Plus 6.0 analysis software was employed for analysis. The number of alveoli and total alveolar area within each field of view were determined, and the ratio of the number of alveoli to the total alveolar area was recorded as the number of alveoli per unit field of view. A crosshair ('+') was drawn at the center of each field of view, and the ratio of its total length to the number of intersecting alveolar septa was noted as the mean lining interval per unit field of view. The difference between the total bronchial area and the bronchial lumen area in each visual field was defined as the percentage of collagen per unit field of view. The ratio of the blue-stained collagen fiber area to the total tissue area within each visual field was recorded as the collagen content. The above analysis process was conducted with the assistance of specialized pathologists.

CT imaging

At 6 months after irradiation, four mice from each group were anesthetized using a continuous ether-oxygen mixture and placed in a small animal CT scanner, and 255 cross-sectional CT scans of the chest were performed. The axial plane was taken at the level of the fifth thoracic vertebra, this is the location where the largest area is photographed, and we chose this location to uniformly

(See figure on next page.)

Fig. 1 The construction and biological characteristics of miR-486-5p-engineered MSC exosomes. **A** Schematic representation of exosome extraction using ultracentrifugation. **B** A representative transmission electron microscopy image of exosomes, with arrows indicating typical exosomes. Scale bar = 200 nm. **C** Nanoparticle tracking analysis of exosomes. **D** Western blot analysis of MSCs (MSC) and MSC-derived exosomes (MSC-Exo). The protein expression of HSP70, CD81, CD63 and TSG101 were detected and GAPDH was used as an internal control. **E** Top 30 small RNAs identified using exosomal sequencing. **F** Green fluorescence infected with gradient multiplicity of infection (MOI) of Ad-GFP-miR-486-5p adenovirus. Scale bar = 200 μm. **G** Expression of miR-486-5p in miR-486-5p-engineered MSC (miR-486-MSC) determined using qPCR. Data are expressed as the mean ± SD. *$p < 0.05$, **$p < 0.01$. **H** Comparison of the proliferation activity of miR-486-MSC and MSC. **I** Identification of CD90, CD73, CD105, CD45, CD34, and CD14 expression on the surface of miR-486-MSC using flow cytometry. **J** Expression of miR-486-5p in miR-486-5p-engineered MSC-exosomes (miR-486-MSC-Exo) compared with MSC-exosomes (MSC-Exo). Data are expressed as the mean ± SD. *$p < 0.05$, **$p < 0.01$

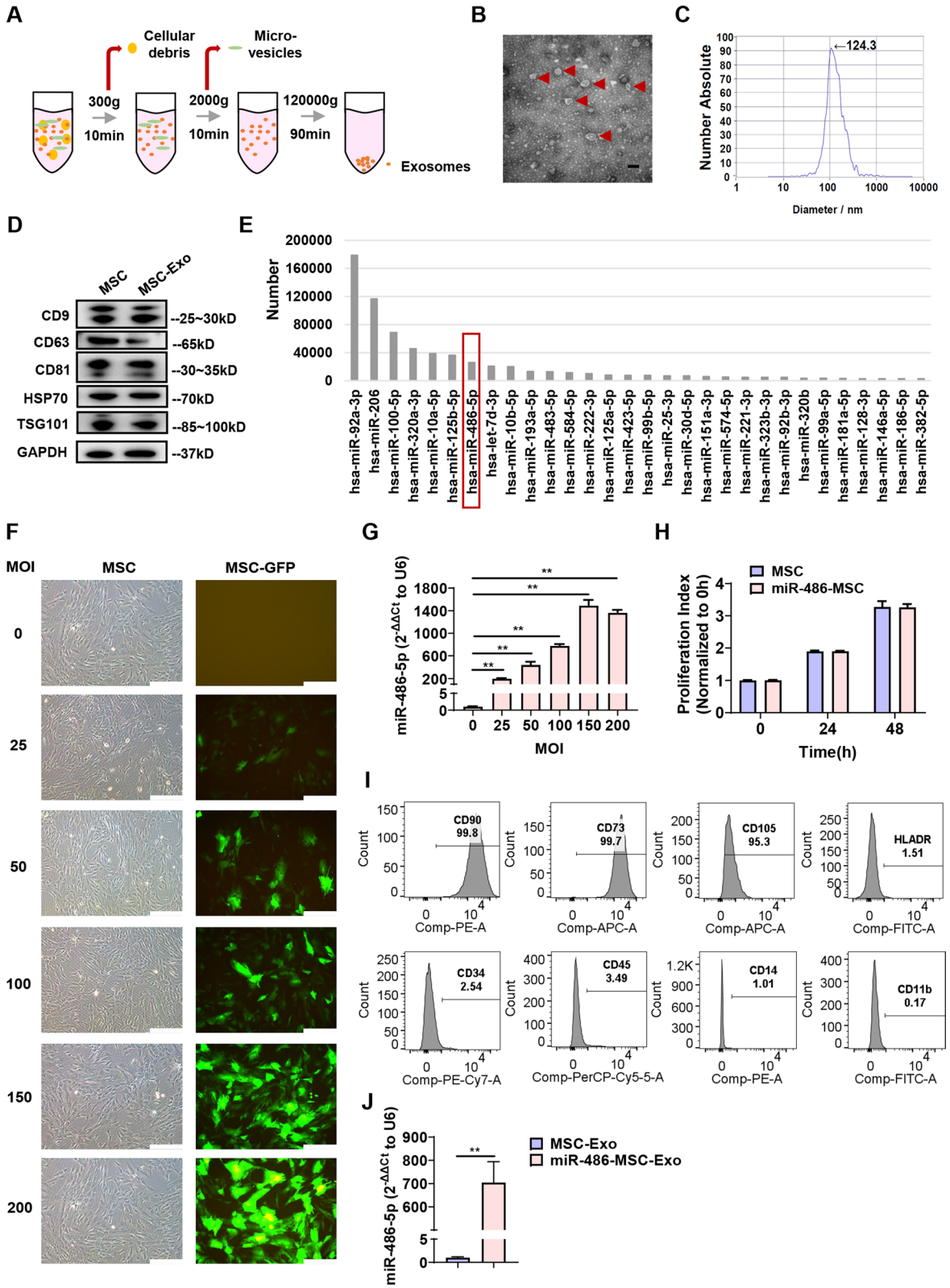

Fig. 1 (See legend on previous page.)

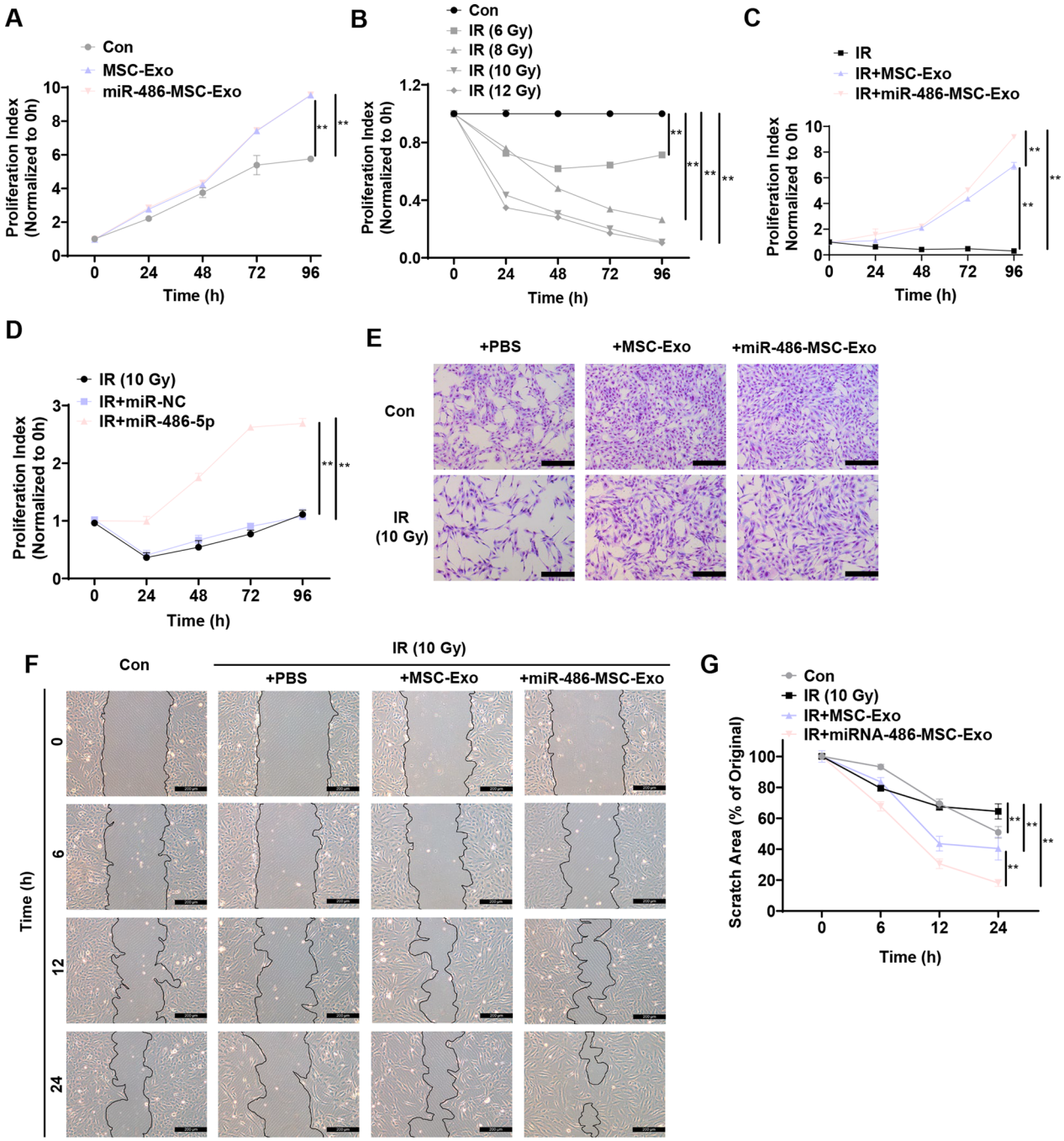

Fig. 2 MiR-486-5p-engineered MSC exosomes increased proliferation and migration of MLE-12 cells after irradiation. **A** Proliferation of MLE-12 cells treated with MSC-Exo or miR-486-MSC-Exo at 0, 24, 48, 72, and 96 h using CCK-8 assay. 1 × PBS was used as the control. Data are expressed as the mean ± SD. *$p < 0.05$, **$p < 0.01$. **B** Proliferation of MLE-12 cells treated with 6, 8, 10, or 12 Gy γ-rays irradiation at 0, 24, 48, 72 and 96 h using CCK-8 assay. 0 h cells were used as control. Data are expressed as the mean ± SD. *$p < 0.05$, **$p < 0.01$. **C** Proliferation of MLE-12 cells treated with MSC-Exo or miR-486-MSC-Exo at 0, 24, 48, 72, and 96 h after irradiation with 10 Gy γ-rays using CCK-8 assay. The irradiated cells served as a control. Data are expressed as the mean ± SD. *$p < 0.05$, **$p < 0.01$. **D** Proliferation of MLE-12 cells transduced with miR-NC or miR-486-5p at 0, 24, 48, 72, and 96 h after irradiation with 10 Gy γ-rays using CCK-8 assay. The irradiated cells served as a control. Data are expressed as the mean ± SD. *$p < 0.05$, **$p < 0.01$. **E** Morphology of MLE-12 cells treated with MSC-Exo or miR-486-MSC-Exo at 48 h after irradiation with 10 Gy γ-rays using Giemsa staining, bar = 200 μm. **F-G** Scratch assay to assess the migration of MLE-12 cells treated with MSC-Exo or miR-486-MSC-Exo. Representative images and quantitative analysis rate at 0, 6, 12, and 24 h were shown. Scale bar = 200 μm. Data are expressed as the mean ± SD. *$p < 0.05$, **$p < 0.01$

shoot mice in order to eliminate the differences caused by different fibrosis in different parts of mice.

Immunofluorescence

After gradient dewaxing and permeability treatment, paraffin sections of mouse lung tissues were treated with sealing solution for 1 h and incubation at 4 ℃ overnight with primary antibodies (rabbit anti-SMAD2, Cell Signaling). they were then incubated with a fluorescent secondary antibody (goat anti-rabbit) at room temperature for 1 h away from light. After the sections were rinsed to remove unbound antibody, the sections were sealed and photographed under a fluorescence microscope. ImageJ software was used to quantify the mean pixel intensity in the red channel, which equates to the ratio of red fluorescence intensity per unit field of view to the cell area, to evaluate the fluorescence signal per unit area.

Transfection and dual luciferase reporter assay

The miR-486-5p mimic (miR-486-5p) and control mimic (miR-NC) were designed and synthesized by Fenghui. Co., Ltd.. MLE-12 cells were seeded in medium without antibiotics overnight before transfection. Transfection at a final concentration of 50 nM was performed using Lipofectamine 2000 (Invitrogen) according to the manufacturer's protocol. At the same time, TGF-β1 (2 ng/mL) was added to each well. After 48 h, the cells were collected for the assays.

Control or miR-486-5p vectors were co-transfected into HEK293 cells with human SMAD2 3 'UTR derived psiCHECK-2 construct (wild type or mutant type) using the same transfection method. The psiCHECK-2 construct is a dual luciferase reporter vector containing two luciferase genes, *Renilla* luciferase and *firefly* luciferase, which can be used as internal controls. The construct derives from human SMAD2 3' UTR that is inserted into the psiCHECK-2 vector, enabling the study of miR-486-5p regulation of SMAD2 gene expression. After transfection for 24 h, luciferase activity was analyzed.

Detection of Akt phosphorylation

MLE-12 cells were cultured and seeded in plates until they reached approximately 60% confluence. MSC-Exo and miR-486-MSC-Exo were added to each well at a concentration of 50 μg/mL, while 1 × PBS was used as the control. After 24 h, insulin was added to each well at a final concentration of 100 nM and incubated at room temperature for 5 min. As an inhibitor group, Ly294002 was added to the wells 1 h before the addition of insulin. The proteins were collected for western blot detection.

Statistical analysis

All values are represented as the mean ± standard deviation. Student's t-test was used for comparisons between two groups, and analysis of variance (ANOVA) was used for comparisons among multiple groups. Differences between groups were considered significant at $p < 0.05$. Use * symbols to represent inter-group significance: * $p < 0.05$, ** $p < 0.01$.

Results

The construction and biological characteristics of miR-486-5p-engineered MSC-exosomes

UC-MSCs were isolated and expanded. Figure 1A shows the preparation procedure for the MSC-derived exosomes. The morphology and particle size distribution of the exosomes were determined using TEM and NTA (Fig. 1B-C). The expression of exosomal marker proteins, such as CD9, CD63, CD81, HSP70, and TSG101, was validated using western blot (Fig. 1D). Exosomal small RNA sequencing revealed that multiple miRNAs, including miR-486-5p, were highly enriched in the exosomes (Fig. 1E). Furthermore, miR-486-5p engineered MSC-exosomes (miR-486-MSC-Exo) were constructed. MSCs were transfected with either miR-486-5p or a control gene via adenovirus-mediated gene transduction. After 48 h, the transfection efficiency and expression of miR-486-5p in MSCs were detected using GFP and qPCR (Fig. 1F-G). The expression of cell surface markers CD90, CD105, CD73, HLADR, CD34, CD45, CD14 and CD11b of both control and miR-486-5p transduced MSCs were detected (Fig. 1H-I, Figure S1). Adenovirus-mediated

(See figure on next page.)

Fig. 3 MiR-486-5p engineered MSC exosomes alleviated erastin-induced ferroptosis in MLE-12 cells. **A** Cell viability of MLE-12 cells treated with increasing doses of erastin (from 0.5 to 8 μM) at 24 h using CCK-8 assay. Data are expressed as the mean ± SD. *$p < 0.05$, **$p < 0.01$. **B** Cell viability (24 h) of MLE-12 cells treated with MSC-Exo or miR-486-MSC-Exo after adding erastin (1 μM) using CCK-8 assay. Fer-1 was used as a positive control. Data are expressed as the mean ± SD. *$p < 0.05$, **$p < 0.01$. **C** Morphological changes (24 h) and **D** divalent iron accumulation (24 h) of MLE-12 cells treated with MSC-Exo or miR-486-MSC-Exo after adding erastin (1 μM) using giemsa staining and divalent iron staining. Fer-1 was used as a positive control. **E** Dihydroethidine (DHE) (24 h) and **F** mitochondrial fluorescence probe (mito-tracker) labeling (24 h) of MLE-12 cells treated with MSC-Exo or miR-486-MSC-Exo after adding erastin (1 μM). Fer-1 was used as a positive control. Scale bar = 10 μm **G-I** mRNA expression (24 h) of GPX4, ACSL4, and SLC7A11 in MLE-12 cells treated with MSC-Exo or miR-486-MSC-Exo after adding erastin (1 μM) using qPCR. Fer-1 was used as a positive control. Data are expressed as the mean ± SD. *$p < 0.05$, **$p < 0.01$

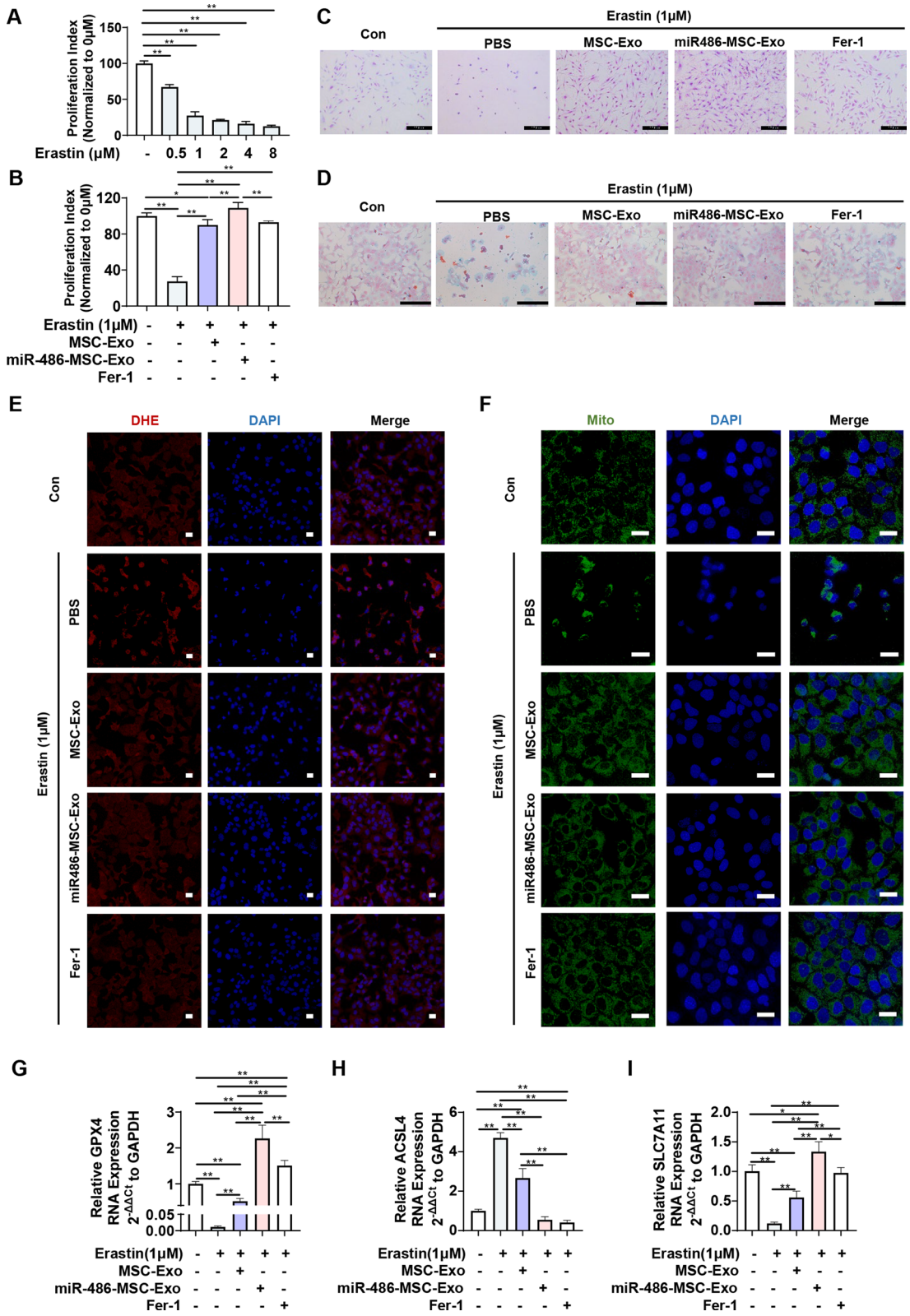

Fig. 3 (See legend on previous page.)

miR-486-5p expression did not affect cell proliferation or expression of cell surface markers. MiR-486-5p-modified MSCs were further cultured, and their supernatants were collected for exosome preparation. The levels of miR-486-5p in exosomes derived from MSCs or miR-486-5p-MSCs were detected using RT-qPCR, and adenoviral vector-mediated miR-486-5p transduction led to an approximately 700-fold increase in miR-486-5p levels in MSC-secreted exosomes (Fig. 1J). Thus, miR-486-MSC-Exo were characterized and analyzed in subsequent experiments.

MiR-486-5p-engineered MSC exosomes enhanced proliferation and migration of MLE-12 cells after IR

MLE-12 cells are commonly used as models of lung injury and fibrotic disease. The cell model of RILI was established by irradiating MLE-12 cells with γ-rays at a dose of 10 Gy. Exosomes or 1 × PBS were added after irradiation or non-irradiation, and cell survival was monitored continuously for 96 h. There were no significant differences in the effects of miR-486-MSC-Exo compared to those of MSC-Exo under normal conditions (Fig. 2A). Treatment with irradiation resulted in a concentration-dependent decrease in the proliferation capacity of MLE-12 cells (Fig. 2B). Correspondingly, the ability of miR-486-MSC-Exo to rescue cells from radiation-induced cell death at 96 h after irradiation was significantly higher than that of MSC-Exo under radiation conditions (Fig. 2C). Compared with miR-NC, miR-486-5p mimic also had a more significant protective effect on radiation-induced lung epithelial cell death at 96 h after irradiation (Fig. 2D). The growth and scratch closure of MLE-12 cells represent their regenerative ability. The ability of miR-486-MSC-Exo to promote proliferation and salvage radiation damage was validated by Giemsa staining (Fig. 2E). At the same time, both miR-486-MSC-Exo and MSC-Exo prevented the loss of lung epithelial migration caused by radiation injury (Fig. 2F-G). At 24 h after scratch, miR-486-MSC-Exo significantly promoted scratch closure compared with MSC-Exo. This suggests that miR-486-MSC-Exo and MSC-Exo can enhance the proliferation and migration of irradiated MLE-12 cells.

MiR-486-5p-engineered MSC exosomes suppressed erastin-induced ferroptosis in MLE-12 cells

Analysis of mRNA expression levels of GPX4, SLC7A11, and ACSL4 in irradiated MLE-12 cells revealed that radiation induced changes in these markers of ferroptosis, indicating that ferroptosis is a form of cell death in radiation injury (Figure S2). MSC-Exo and miR-486-MSC-Exo demonstrated significant intervention effects on these changes, suggesting a potential reduction of radiation injury by inhibiting ferroptosis. An erastin-induced lung epithelial MLE-12 cell ferroptosis model was confirmed by a gradual decrease in cell viability (Fig. 3A). MiR-486-MSC-Exo and MSC-Exo suppressed erastin-induced ferroptosis in MLE-12 cells, but miR-486-MSC-Exo exhibited stronger activity than that of MSC-Exo and the positive control (Fer-1; Fig. 3B). Giemsa staining and divalent iron staining showed that miR-486-MSC-Exo and MSC-Exo maintained the morphology of ferroptosis cells and prevented intracellular divalent iron accumulation (Fig. 3C-D). DHE staining revealed that both miR-486-MSC-Exo and MSC-Exo decreased the accumulation of peroxide anions in the cytoplasm of ferroptosis cells (Fig. 3E, S3A). Mito-tracker staining revealed that both miR-486-MSC-Exo and MSC-Exo reversed erastin-induced mitochondrial shrinkage (Fig. 3F, S3B). qPCR further clarified changes in the expression of ferroptosis markers (GPX4, ACSL4, and SLC7A11) in erastin-treated MLE-12 cells. Results showed that miR-486-MSC-Exo and MSC-Exo reversed characteristics of ferroptosis in MLE-12 cells (Fig. 3G-I). This suggests that miR-486-MSC-Exo prevents lung epithelial cell death in vitro, partially by rescuing cells from ferroptosis.

MiR-486-5p-engineered MSC exosomes suppress fibrosis-related gene expression in MLE-12 cells

After induction of ferroptosis in MLE-12 cells with erastin (1 μM) for 6 h, a 24 h-culture supernatant was collected and then transferred to newly laid MLE-12 cells for co-culture. Cells were collected after 24 h, 48 h, and 72 h of co-culture to determine mRNA expression levels (Fig. 4A). The results of qPCR showed that erastin induced the up-regulated expression of fibrosis-related genes, including FN, αSMA, SMAD2 and CTGF, suggesting a link between ferroptosis and fibrosis (Fig. 4B).

(See figure on next page.)

Fig. 4 MiR-486-5p-engineered MSC exosomes reduce pulmonary fibrosis in vitro. **A-B** mRNA expression of FN, αSMA, SMAD2, and CTGF in MLE-12 cells treated with erastin-induced supernatant at 24 h, 48 h, and 72 h via qPCR. Data are expressed as the mean ± SD. *$p < 0.05$, **$p < 0.01$. **C** mRNA expression of FN, αSMA, SMAD2, and CTGF in MLE-12 cells treated with gradient concentrations (0, 1, 2, 4 ng/mL) of TGF-β1. Data are expressed as the mean ± SD. *$p < 0.05$, **$p < 0.01$. **D** mRNA expression of FN, αSMA, SMAD2, and CTGF in MLE-12 cells treated with MSC-Exo or miR-486-MSC-Exo after adding TGF-β1 (2 ng/mL). Data are expressed as the mean ± SD. *$p < 0.05$, **$p < 0.01$. **E-L** Protein expression and quantitative analysis of FN, αSMA, SMAD2, and CTGF in MLE-12 cells with MSC-Exo or miR-486-MSC-Exo after adding TGF-β1 (2 ng/mL), with GAPDH as the internal reference. Data are expressed as the mean ± SD. *$p < 0.05$, **$p < 0.01$

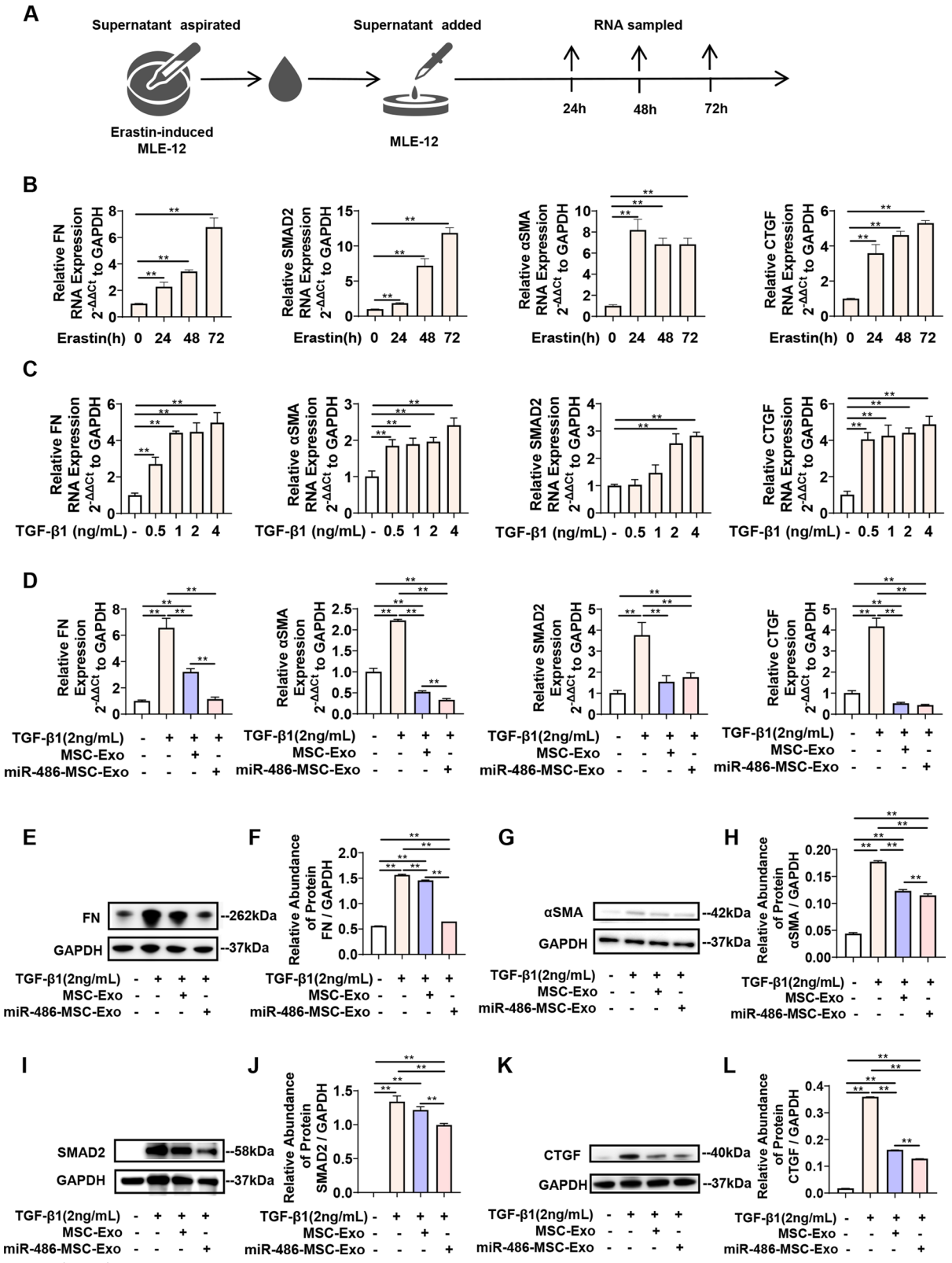

Fig. 4 (See legend on previous page.)

To explore whether miR-486-MSC-Exo and MSC-Exo have regulatory effects on fibrosis, TGF-β1-treated MLE-12 cells were generated as a fibrosis model. Treatment with TGF-β1 resulted in the up-regulated expression of fibrosis-related genes, FN, αSMA, SMAD2, and CTGF, in MLE-12 cells in a concentration-dependent manner (Fig. 4C). Both miR-486-MSC-Exo and MSC-Exo strongly reduced the TGF-β1-induced expression of the mRNA of these fibrosis genes (Fig. 4D). Among them, compared with MSC-Exo, miR-486-MSC-Exo significantly down-regulated the mRNA expression levels of FN and αSMA induced by TGF-β1. Western blot analysis showed that both miR-486-MSC-Exo and MSC-Exo could significantly reduce the expression levels of TGF-β1-induced fibrotic proteins, including FN, SMAD2 and CTGF (Fig. 4E-L). Compared with MSC-Exo, miR-486-MSC-Exo significantly down-regulated the protein expression levels of FN, SMAD2 and CTGF induced by TGF-β1. The original protein expression level of αSMA was very low in MLE-12 cells. Both MSC-Exo and miR-486-MSC-Exo could moderately suppress the expression level of TGF-β1-induced αSMA protein, whereas their significance was slight. These results indicate the ability of miR-486-MSC-Exo to suppress fibrotic gene expression in MLE-12 cells.

MiR-486-5p-engineered MSC exosomes ameliorate inflammatory responses and fibrosis in RILI mice

To evaluate the therapeutic effect of miR-486-MSC-Exo on RIPF in vivo, the chests of mice were irradiated with γ-rays at a dose of 20 Gy. MSC-Exo, miR-486-MSC-Exo and 1×PBS were administered intravenously after irradiation, and changes in survival rate, body weight, inflammatory factor levels, and pathology of mice were evaluated. An outline of the experimental process is shown in (Fig. 5A). The survival of the mice injected with exosomes or 1×PBS after IR were measured (Fig. 5B). The results showed that the death of mice in the IR group occurred one month after IR, which may be related to lung dysfunction and excessive fibrosis in the mice. In comparison, the groups administered MSC-Exo or miR-486-MSC-Exo had a high survival rate, especially no death occurred in miR-486-MSC-Exo-treated group. This highlights the efficacy of exosomes in the treatment of RIPF and suggests a therapeutic role for miR-486-5p in pulmonary fibrosis. Neither exosomes nor 1×PBS affected mouse weight during the experiments (Fig. 5C). Measurements of inflammatory factors in BALF showed that radiation injury resulted in increased IL-6, TNF-α, and IL-18 levels in mice, while exosome administration significantly inhibited the increase of these inflammatory factors (Fig. 5D-F). MiR-486-MSC-Exo significantly reduced TNF-α levels compared with MSC-Exo on day 28 after treatment, suggesting supper anti-inflammatory effects. According to the analysis results in (Fig. 5H-K), the irradiated lung tissue showed obvious histological changes from 1 to 6 months post-IR, including the reduction of alveoli number, the increase of mean lining interval, the thickening of total bronchial wall, and the increase of collagen deposition, which were significantly alleviated by treatment with miR-486-MSC-Exo and MSC-Exo. Among them, miR-486-MSC-Exo, compared with MSC-Exo, significantly reduced the total bronchial wall area at 3 months post-irradiation, and significantly increased the number of alveoli and decreased the percentage of collagen at 6 months post-IR. These results indicate that miR-486-MSC-Exo can improve the survival rate of RILI mice and reduce radiation-induced inflammatory infiltration and pulmonary fibrosis.

Construction of hACE2$^{CKI/CKI}$ Sftpc-Cre^{+} mice and distribution of exosomes directed by RBD- miR-486-5p in vivo.

MSC-derived exosomes modified with SARS-CoV-2-S-RBD (RBD-MSC-Exo) and exosomes double-modified with SARS-CoV-2-S-RBD and miR-486-5p (miR-486-RBD-MSC-Exo) were prepared by adenovirus modification of MSCs (Fig. 6A). Western blot confirmed positive expression of RBD protein in RBD-MSC and RBD-MSC-Exo (Fig. 6B). hACE2 conditional knock-in mice were constructed, and pulmonary hACE2 mice (hACE2$^{CKI/CKI}$ Sftpc-Cre^{+} mice) were obtained by hybridization with the lung-specific promoter Cre^{+} mice (Sftpc-Cre^{+} mice) (Fig. 6C). The genotypes of the homozygous and heterozygous mice produced by crossbreeding were identified using the mouse tail gene (Fig. 6D). Western blot

(See figure on next page.)

Fig. 5 MiR-486-5p engineered MSC exosomes reduce pulmonary fibrosis in vivo. **A** Schematic representation. **B** Survival curves and **C** body weight changes of RIPF mice treated with MSC-Exo or miR-486-MSC-Exo, with nine mice in each group. 1×PBS was used as negative control. **D-F** Expression of IL-6, TNF-α, and IL-18 in the bronchoalveolar lavage fluid (BALF) of RIPF model mice treated with MSC-Exo or miR-486-MSC-Exo via ELISA. Data are expressed as the mean ± SD. *$p < 0.05$, **$p < 0.01$. **G** Representative images of H&E and Masson staining at 1 M, 3 M, or 6 M in RIPF mice treated with MSC-Exo or miR-486-MSC-Exo, with four mice in each group. 1×PBS was used as negative control. The red, green, and orange arrows indicate alveoli, bronchial walls, and collagen, respectively. Scale bar = 200 μm. **H–K** Statistical analysis of H&E and masson, including number of alveoli per unit field of view, mean lining interval per unit field of view, total bronchial wall area per unit field of view, and percentage of collagen per unit field of view. Data are expressed as the mean ± SD. *$p < 0.05$, **$p < 0.01$

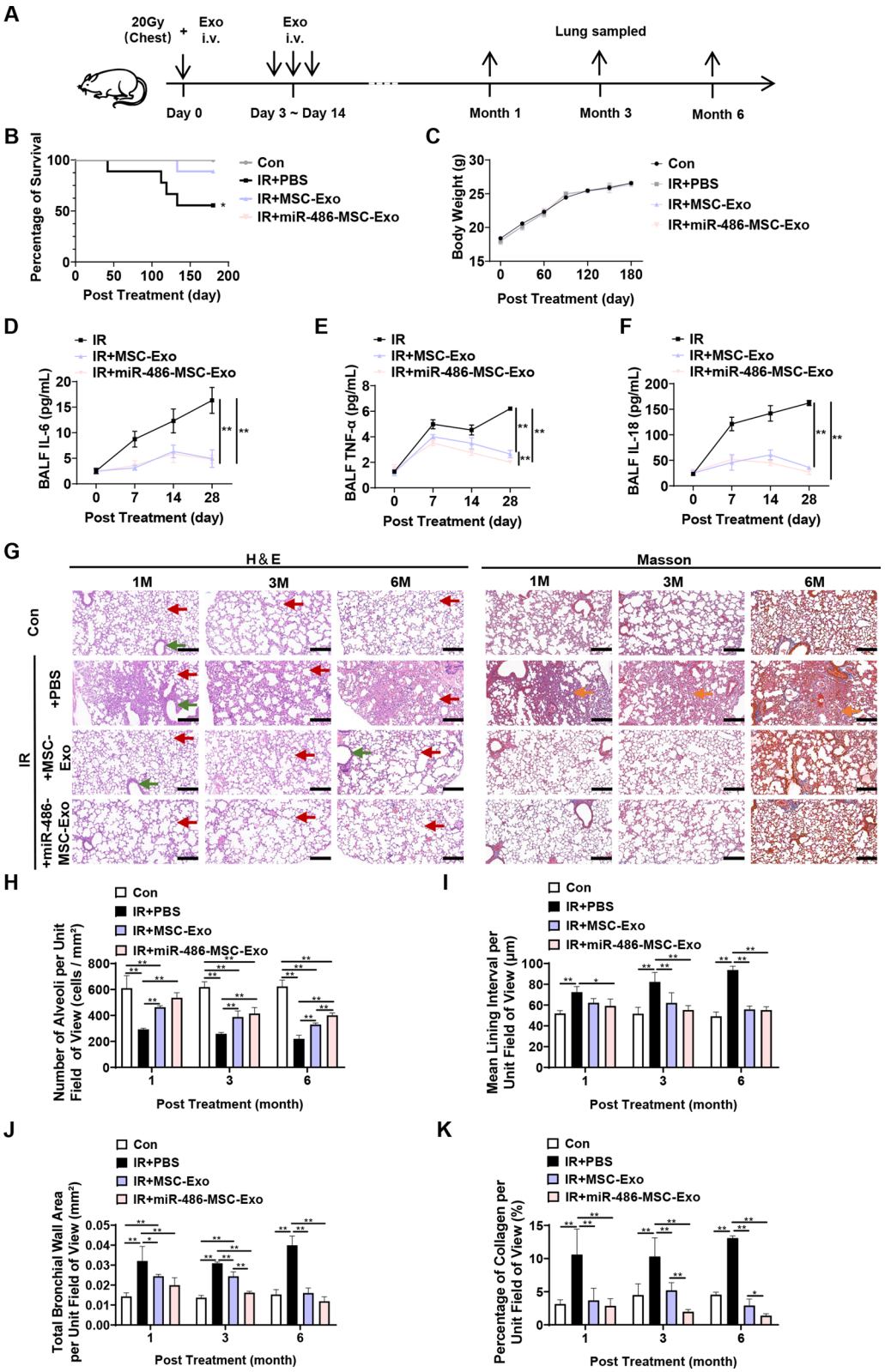

Fig. 5 (See legend on previous page.)

confirmed the high expression of hACE2 in the lung tissues of hACE2$^{CKI/CKI}$ Sftpc-Cre^{+} mice induced by tamoxifen (Fig. 6E). This provided a model for evaluating the distribution of RBD- MSC-derived exosomes in vivo. Based on this model, the effect of MSC-derived exosomes in the treatment of RIPF through targeted delivery of miR-486-5p was evaluated.

After labeling with DiR dye, RBD-miR-486-5p exosomes and scramble-miR-486-5p exosomes were injected into hACE2$^{CKI/CKI}$ Sftpc-Cre^{+} mice through the tail vein, namely RBD-group and Scramble-group, and the organ distribution of the exosomes in hACE2$^{CKI/CKI}$ Sftpc-Cre^{+} mice was measured. The results showed that after intravenous administration, most of the exosomes were first distributed to the lungs and liver via the circulatory system (Fig. 6F-I). On and after day 3 of administration, the ratio of lung radiation efficiency in the RBD-group was significantly increased compared with the Scramble-group, which means that the exosomal modification of RBD can achieve the retention of exosomes in lung tissue.

MiR-486-5p engineered MSC exosomes improved therapeutic efficiency for pulmonary fibrosis through the targeted binding of RBD-hACE2

The therapeutic effect of the miR-486-RBD-MSC-Exo on RIPF in vivo was explored using hACE2$^{CKI/CKI}$ Sftpc-Cre^{+} mice. Exosomes or 1 × PBS were administered intravenously to RIPF mice after irradiation, and changes in survival rate, body weight, pathology and imaging changes of mice were evaluated. The experimental procedure is shown in Fig. 7A. Survival curves were generated, and the therapeutic effects of exosomes were assessed (Fig. 7B). The results showed that mice in the irradiated group (IR + PBS) died after the first month of irradiation and exhibited a survival rate of only 55%. Correspondingly, the survival rates of the MSC-Exo, miR-486-MSC-Exo, RBD-MSC-Exo-treated groups were 88%. In particular, no mouse deaths occurred in the miR-486-RBD-MSC-Exo group. Neither exosomes nor 1 × PBS affected mouse weight during the experiments (Fig. 7C). Pathological analysis of lung tissues was performed, and scanning photos (Fig. 7D) and analysis results (Fig. 7E-H) showed significant histological changes in the lung tissue of the IR + PBS group at 6 months post-IR, including a decrease in the number of alveoli, an increase in the mean lining interval, thickening of the total bronchial wall, and an increase in collagen deposition. Although the above symptoms were slightly relieved after treatment with MSC-Exo, treatment with miR-486-MSC-Exo significantly increased the number of alveoli. Treatment with RBD-MSC-Exo significantly reduced the mean liner interval. In contrast, the treatment of miR-486-RBD-MSC-Exo exhibited a more significant effect on increasing the number of alveoli, reducing the mean lining interval, the total bronchial wall thickness, and collagen deposition. CT imaging revealed similar results, with live CT of RIPF mice showing a gray-like lesion at the lung edge, which suggests fibrosis. However, the images of the lungs in the RIPF groups administered exosomes showed clear lung boundaries (Fig. 7I). These results indicated that miR-486-RBD-MSC-Exo improved survival and inhibited pulmonary fibrosis in RIPF mice.

MiR-486-5p engineered MSC exosomes alleviate pulmonary fibrosis via miR-486-5p-SMAD2-Akt phosphorylation

The therapeutic effect of miR-486-RBD-MSC-exosomes in RIPF in hACE2$^{CKI/CKI}$ Sftpc-Cre^{+} mice was investigated using the procedure shown in Fig. 7. Immunofluorescence of lung tissue sections revealed significantly higher SMAD2 expression in RIPF mice compared to that in control mice (Fig. 8A-B), which was not improved following the administration of MSC-Exo or RBD-MSC-Exo. However, SMAD2 levels were significantly reduced in the miR-486-MSC-Exo- and miR-486-RBD-MSC-Exo-treated groups, suggesting that exosomes modified with miR-486-5p can significantly reduce irradiation-induced pulmonary fibrosis in vivo through SMAD2.

We further studied the regulatory mechanism of miR-486-5p in SMAD2 expression. In vitro experiments showed that an miR-486-5p mimic reduced SMAD2 mRNA (Fig. 8C) and protein expression (Fig. 8D-E) in TGF-β1-treated MLE-12 cells. Accordingly, the interaction targets of miR-486-5p and SMAD2 were screened, and it was found that miR-486-5p had specific targets in both the human and mouse SMAD2 3'UTR (Fig. 8F). HEK293 cells containing the human SMAD2 3 'UTR

(See figure on next page.)

Fig. 6 Exosomes can achieve targeted lung delivery in vivo via RBD-hACE2. **A** Structure diagram of RBD-miR-486-5p engineered exosomes (miR-486-RBD-MSC-Exo). **B** Western blot analysis of RBD protein expression in RBD-MSC and RBD-MSC-Exo, with MSC as a comparison. GAPDH was used as the internal reference. **C** Construction diagram of hACE2$^{CKI/CKI}$ -SftpcCre^{+} mice. **D** Genotype identification of hACE2$^{CKI/CKI}$ -SftpcCre^{+} mice. **E** Western blot analysis of hACE2 expression in hACE2$^{CKI/CKI}$ -SftpcCre^{-} mice and hACE2$^{CKI/CKI}$ -SftpcCre^{+} mice with tamoxifen induction. β-actin was used as the internal reference. **F** Early organ distribution of miR-486-RBD-MSC-Exo bound to DiR after intravenous administration in hACE2$^{CKI/CKI}$ -SftpcCre^{+} mice. Scramble-miR-486-5p engineered exosomes (miR-486-Scamble-MSC-Exo) was used as control. **G-I** Quantitative analysis of fluorescence distribution from E. Data are expressed as the mean ± SD. *$p < 0.05$, **$p < 0.01$

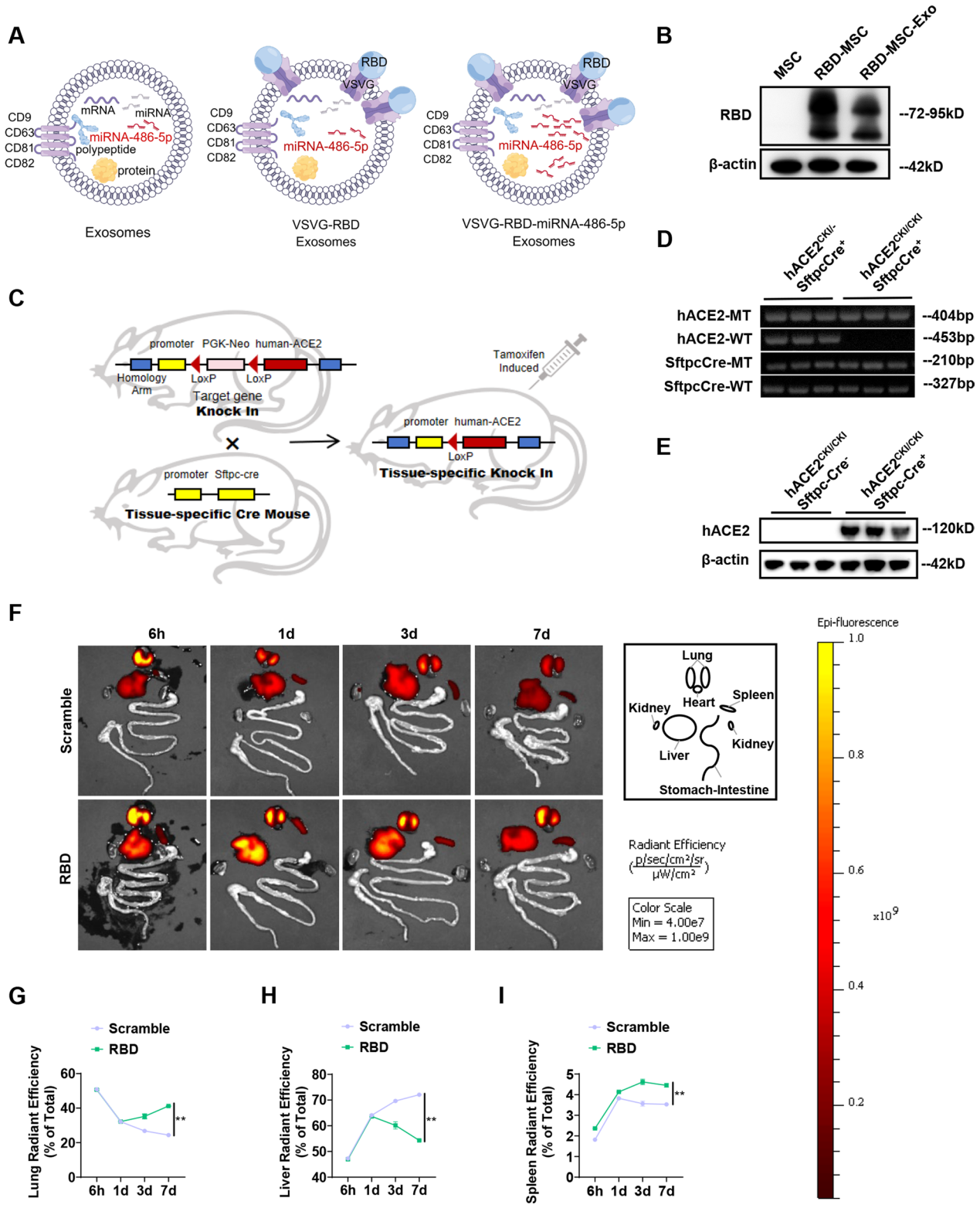

Fig. 6 (See legend on previous page.)

derived psiCHECK-2 construct (wild-type or mutant) were transfected with miR-486-5p or miR-NC, and the cells were harvested and analyzed for luciferase activity (Fig. 8G). The over-expression of miR-486-5p significantly reduced the expression level of SMAD2 in the wild-type construct but not in the mutant type, indicating that miR-486-5p targeted SMAD2 gene expression.

At the same time, we explored the role of the Akt pathway in the regulation of SMAD2 by miR-486-5p. A classic insulin (5 min) -induced Akt phosphorylation model was established, and western blot was used to verify protein expression related to total Akt and Akt phosphorylation (p Akt) in the presence of MSC-Exo and miR-486-MSC-Exo (Fig. 8H-J). The results showed that miR-486-MSC-Exo significantly increased Akt phosphorylation, which was inhibited by the Akt phosphorylation inhibitor LY294002 (Cell Signaling Technology). This proves that miR-486-5p is involved in the repair of pulmonary fibrosis by activating Akt phosphorylation and targeting SMAD2.

Discussion

MSC-derived exosomes have shown the regenerative effects against lung injury including RILF [36]. Gene engineering could improve the regenerative activity of MSC derived-exosomes by changing their biological characteristics and increasing their effector levels. Based on the interaction of SARS-CoV-2-S-RBD with ACE2, we developed an engineered MSC-exosomes carrying miR-486-5p to intervene in RIPF. ACE2 is a receptor protein found on the surface of many cell types and is highly expressed in the human lungs. Single-cell sequencing reveals that ACE2 is mainly expressed in type II alveolar, vascular endothelial, and mesenchymal cells, which are sensitive to radiation injury [15]. ACE2 expression is up-regulated in alveolar cells in injury or inflammatory conditions and contributes to epithelial-mesenchymal transition [37]. Furthermore, ACE2 activation can inhibit the inflammatory response, apoptosis, and pulmonary fibrosis. Thus, $ACE2^{+}$ cells are ideal targets for engineered MSC-exosomes to interference RILF. ACE2 is identified as the recognition receptor for SARS-CoV-2, and can be carried by exosomes to act as a vaccine candidate against COVID-19 [12, 13]. ACE2 interacts with RBD of the SARS-CoV-2 spike protein to form a complex which promotes its crystallization [38, 39]. Exosomes with high RBD levels have been shown activity to block SARS-CoV-2 infections and protect $ACE2^{+}$ cells [35, 40]. Thus, engineered MSC-derived exosomes based on the interaction between the SARS-CoV-2-S-RBD and ACE2 were able to target $ACE2^{+}$ cells and lung. ACE2 is also abundant in small intestines and kidneys of humans, potentially leading to the distribution of RBD-engineered exosomes in organs beyond the lungs. Even ACE2 targeted exosomes can be distributed in other organs, it has significant advantages in the treatment of traumatic lung diseases, because ACE2 protein is an inflammation response gene and upregulated in the injured lung [16].

RIPF is a complex pathological process in which radiation induces reactive oxygen species (ROS) production and activates fibroblasts to excessive deposition of the extracellular matrix [41, 42]. Dysregulated cell activation and proliferation of complex cell populations such as epithelial cells and fibroblasts in the lungs, is one of the hallmarks of pulmonary fibrosis. Tissue damage signals associated with cell death, senescence and inflammation cause deregulated epithelial cell proliferation and activation, whereas MSC- derived exosomes provide stimulating signals to promote regeneration in injured lung tissues. MSC-derived exosomes repair tissue damage by suppressing inflammation and fibrosis [43, 44] and are considered ideal drug delivery for intervention RIPF [11]. However, the distribution characteristics of MSC-derived exosomes limit their delivery efficacy to lung and effectiveness in the treatment of lung diseases through systemic administration. MSC-derived exosomes have different distribution dynamics compared to MSCs [45, 46]. Intravenously administrated MSC-derived exosomes initially accumulate in the liver, whereas MSCs initially accumulate in the lungs [45, 46].

(See figure on next page.)

Fig. 7 The targeted binding of RBD-hACE2 in miR-486-5p-engineered MSC exosomes enhance treatment efficacy for pulmonary fibrosis. **A** Schematic representation. **B** Survival curves of $hACE2^{CKI/CKI}$ -$SftpcCre^{+}$ mice treated with MSC-Exo, miR-486-MSC-Exo, RBD-MSC-Exo and miR-486-RBD-MSC-Exo after irradiation, with nine mice in each group. 1 × PBS was used as negative control. **C** Body weight changes of RIPF mice treated with MSC-Exo or miR-486-MSC-Exo, with nine mice in each group. 1 × PBS was used as negative control. **D** Representative images of H&E and Masson staining at 6 M in RIPF $hACE2^{CKI/CKI}$ -$SftpcCre^{+}$ mice treated with MSC-Exo, miR-486-MSC-Exo, RBD-MSC-Exo and miR-486-RBD-MSC-Exo, with four mice in each group. 1 × PBS was used as negative control. Scale bar = 200 μm. **E–H** Statistical analysis of H&E and masson, including number of alveoli per unit field of view, mean lining interval per unit field of view, total bronchial wall area per unit field of view, and percentage of collagen per unit field of view. The red, green, and orange arrows indicate alveoli, bronchial walls, and collagen, respectively. Data are expressed as the mean ± SD. $*p < 0.05$, $**p < 0.01$. **I** Representative small animal CT images in RIPF $hACE2^{CKI/CKI}$ -$SftpcCre^{+}$ mice treated with MSC-Exo, miR-486-MSC-Exo, RBD-MSC-Exo and miR-486-RBD-MSC-Exo. The red arrow indicates areas of fibrosis. 1 × PBS was used as negative control

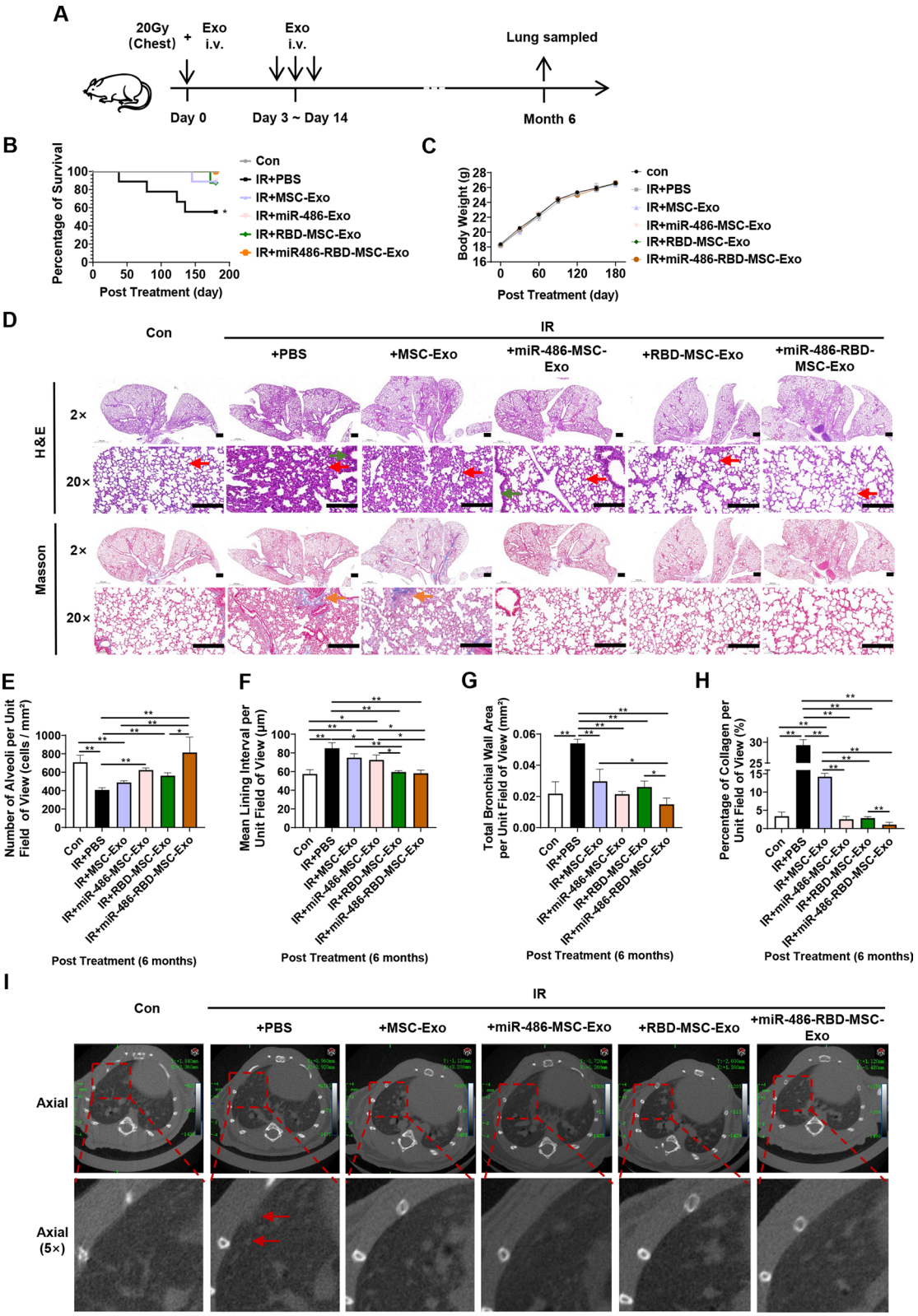

Fig. 7 (See legend on previous page.)

Engineered MSC-exosomes could achieve lung retargeting and improve regenerative efficiency in lung injury through modification based on interactions of biological molecules.

MSC-derived exosomes modified with SARS-CoV-2-S-RBD were validated to be enriched in the lungs after intravenous administration. Because the mice are not susceptible to SARS-CoV-2 due to ACE2 differences, the distribution and therapeutic efficacy of MSC-derived exosomes containing the RBD was evaluated by using human ACE2 transduced hACE2$^{CKI/CKI}$ Sftpc-Cre^{+} mice. Multiple studies have reported that MSC-derived exosomes can deliver miRNAs to cells and act as vehicles to carry anti-inflammatory and anti-fibrotic small-molecule drugs into lung tissues to alleviate RIPF [47, 48]. Thus, MSC-derived exosomes modified with SARS-CoV-2-S-RBD could function as a targeted delivery system of effectors such as miRNAs for RIPF treatment. Although drug delivery routes for lung diseases vary, including oral, intravenous, inhalant, intratracheal [49], these retargeted MSC-derived exosomes have the remarkable advantages for RIPF because of their high bioavailability and direct delivery of biologics to the microvascular endothelial cells and bronchial epithelial cells.

MSC-derived exosomes contain a vast quantity of small RNAs which play crucial roles intercellular communication and tissue regeneration. Analysis of miRNA profiles of MSC-derived exosomes focused on the highly expressed small RNAs and indicate their potential roles in biological activities. Among them, miR-486-5p is a multifunctional miRNA and was first identified in hematopoietic fetal liver tissue [50]. MiR-486-5p also acts as a regulator to regulate cell proliferation, migration, angiogenesis, apoptosis, erythroid differentiation, and drug resistance [51–55]. Extensive studies have revealed that miR-486-5p is involved in the regulation of oxidative damage resistance and the inhibition of collagen hyperproliferation, and fibrosis [56–58]. MiR-486-5p down-regulation was observed in the serum and lung tissues of patients with silicosis and idiopathic pulmonary fibrosis [21]. Additionally, miR-486-5p attenuates pulmonary fibrosis in mouse models exposed to silica or bleomycin [21]. Based on MSCs miRNA profile and biological activity, miR-486-5p was considered as an ideal effector for engineered MSC-exosomes to intervene RIPF. Adenovirus treatment of MSCs resulted in a more than 700-fold increase in miR-486-5p expression in MSC-derived exosomes. Thus, genetically modified MSCs with miR-486-5p and membrane-loaded S-RBD could develop a lung-retarget MSC-exosomes enriched miR-486-5p, which have potential as a novel therapeutic approach to RILI and alleviate RIPF.

The pathological features of fibrosis are associated with the accumulation of extracellular matrix in the affected tissues. Dysregulated cell activation and proliferation of complex cell populations such as epithelial cells, MSCs, fibroblasts, immune cells, and endothelial cells in the lung is one of the key hallmarks of pulmonary fibrosis. Usually, signals associated with cell death, senescence and inflammation cause deregulated epithelial cell proliferation and activation, whereas regenerative signals from MSCs-derived exosomes promote proliferation that plays a regenerative role in injured lung tissues. Ionization leads to cell death and secondary inflammation, which are critical processes in radiation-induced fibrosis. Erastin is a potent, metabolically stable inducer of ferroptosis [59]. By using radiation and erastin-induced ferroptosis models of alveolar epithelial cells, the suppressive effects of miR-486-5p-engineered MSC exosomes on ferroptosis were validated in this study. Even MSC-derived exosomes on ferroptosis and liver fibrosis have been respectively reported [60, 61], the mechanisms that engineered MSC-exosomes suppress alveolar epithelial cell ferroptosis and secondary fibrosis still remain novelty. TGF-β1 is a central mediator of fibrogenesis. Ferroptosis inhibitors, such as liproxstatin-1, attenuates radiation-induced

(See figure on next page.)

Fig. 8 MiR-486-5p-engineered MSC exosomes alleviates pulmonary fibrosis via miR-486-5p-SMAD2-pAkt. **A** SMAD2 protein expression in lungs of RIPF hACE2$^{CKI/CKI}$ -SftpcCre^{+} mice at 6 M after irradiation via immunofluorescence, with four mice in each group. Representative images were shown. Scale bar = 200 μm. **B** Fluorescent quantitation of SMAD2 protein expression (red) in RIPF mice treated with different exosomes. Data are expressed as the mean ± SD. *$p < 0.05$, **$p < 0.01$. **C** mRNA and **D-E** protein expression of SMAD2 in MLE-12 cells treated with miR-486-5p mimic (miR-486-5p) after adding TGF-β1 (2 ng/mL). MiR-NC was used as control. Data are expressed as the mean ± SD. *$p < 0.05$, **$p < 0.01$. **F** MiR-486-5p target site in the SMAD2 3′UTR and the sequence alignment of miR-486-5p and the SMAD2 3′UTR. Mutated bases in the psiCHECK-2 construct are bold. **G** Luciferase activity after co-transfection of miR-486-5p and SMAD2 into HEK293 cells. MiR-NC was used as a control. Renilla luciferase activity was normalized to firefly luciferase activity. Data are expressed as the mean ± SD. *$p < 0.05$, **$p < 0.01$. **H-J** Western blot analysis of Akt phosphorylation in MLE-12 cells treated with MSC-Exo or miR-486-MSC-Exo. Insulin was used as an inducer of Akt phosphorylation. LY294002 was used as an inhibitor of Akt phosphorylation. Data are expressed as the mean ± SD. *$p < 0.05$, **$p < 0.01$

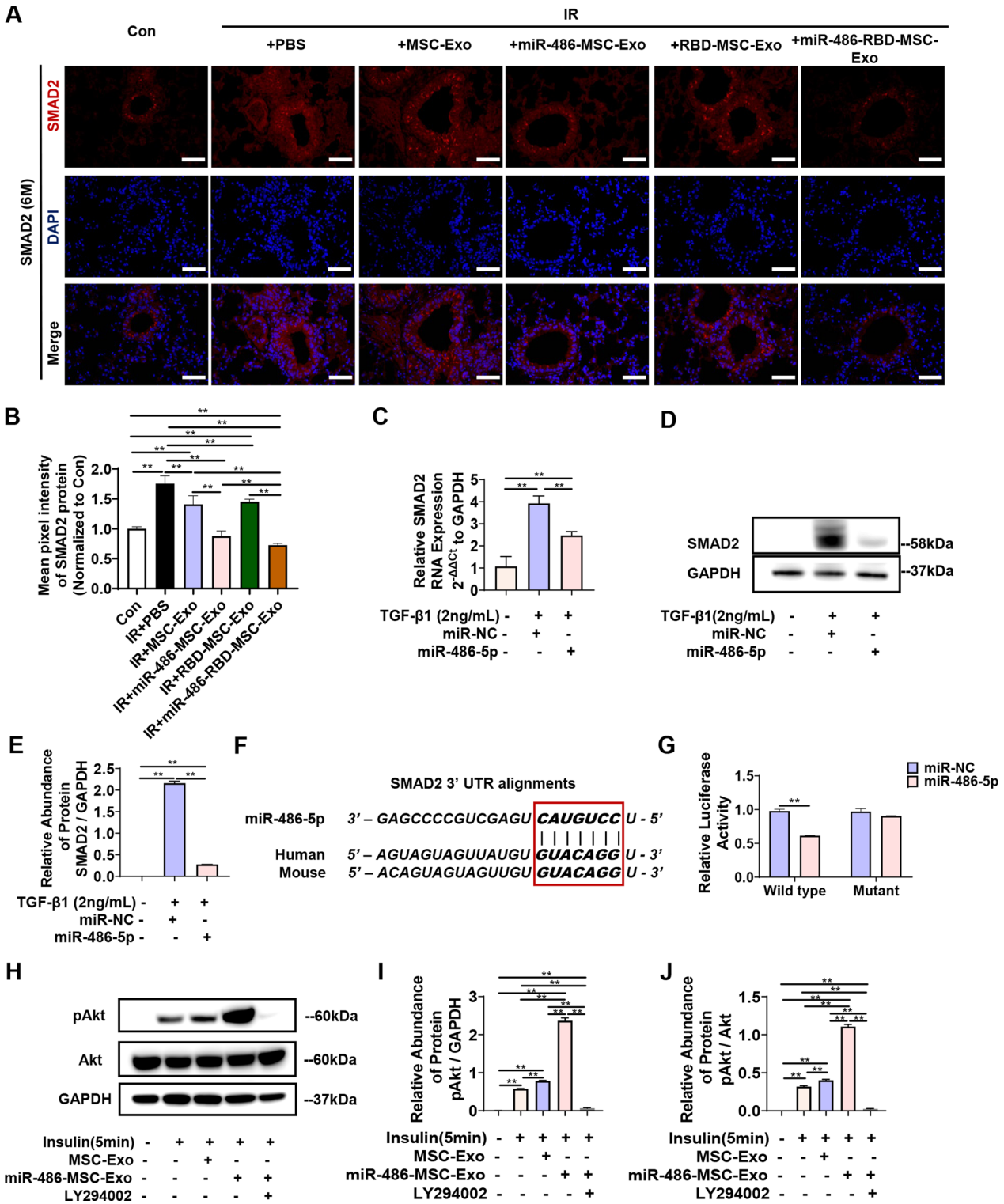

Fig. 8 (See legend on previous page.)

pulmonary fibrosis by modulating GPX4 and inhibiting TGF-β1 signaling [62]. By measuring fibrosis gene expression in alveolar epithelial cells treated with supernatant of ferroptosis cells in vitro, we provide the direct evidence that ferroptosis links fibrosis and miR-486-MSC-Exo intervene fibrosis through suppressing ferroptosis. Furthermore, miR-486-RBD-MSC-Exo improved survival and inhibited pulmonary fibrosis in a ACE2 humanized mouse model, in which miR-486-RBD-MSC-Exo had increased distribution in the lungs. Comprehensive assessment of radiation-induced lung tissue damage and therapeutic effects of exosomes should consider multiple indicators including changes in survival rates, weight, early cytokine changes, and full-course pathological changes. Even association between weight loss and mortality in idiopathic pulmonary fibrosis were observed both in clinical and chemical-induced animal models [63], the weight loss was not significant in this mouse RILI model in which local chest was irradiated. However, miR-486-RBD-MSC-Exo exhibited a more significant effect on improving the pathological changes such as increasing the number of alveoli, reducing the mean lining interval and collagen deposition. Both the in vitro and in vivo data support the conclusion that miR-486-RBD-MSC-Exo suppress fibrosis by suppressing ferroptosis.

The identification of miRNA-mRNA target interactions is fundamental for elucidating the regulatory network governed by miRNAs. Validated miR-486-5p targets include phosphatase and tensin homolog (PTEN) and FoXO1, whose suppression activates phosphatidyl inositol-3-kinase (PI3K) /Akt signaling [64]. MiR-486-5p inhibits transforming growth factor (TGF)-β via targeting Smad1/2/4 and IGF-1. Other miR-486-5p targets include matrix metalloproteinase-19 (MMP-19), Sp5, histone acetyltransferase 1 (HAT1), and nuclear factor of activated T cells-5 (NFAT5) [64]. Among the predicted and validated targets network of miR-486-5p, PI3K/Akt is a highly conserved signal transduction network in eukaryotic cells that plays a crucial role in tissue regeneration. Transforming growth factor-β1 (TGF-β1) is considered as a crucial mediator in tissue fibrosis and regulated by Smads. Thus, the akt activation and SMAD2 expression in miR-486-RBD-MSC-Exo treated cells were validated. Even Akt pathway is fibrosis pathogen in fibroblast and macrophages, its activation is critical for tissue regeneration in RILI [65]. MiR-486-5p activates the Akt signaling pathway in human endothelial cells for repair ischemic kidney injury [66, 67]. Thus miR-486-5p mediated the activation of Akt might contribute to regenerative effect of miR-486-MSC-Exo. Furthermore, the interaction targets of miR-486-5p and SMAD2 were validated, and SMAD2 miR-486-5p-SMAD2 regulatory networks were identified in the TFG-β1-induced cell models. MiR-486-MSC-Exo alleviate radiation-induced lung injury and long-term pulmonary fibrosis through suppressing ferroptosis. The retarget engineered MSC-exosomes might be an effective approach for intervention RIPF.

Conclusion

We developed an engineered MSC exosomes with SARS-CoV-2-S-RBD- and miR-486-5p-modification. MiR-486-RBD-MSC-Exo significantly suppress ferroptosis and fibrosis of lung epithelial cells in vitro, alleviate radiation-induced lung injury and long-term pulmonary fibrosis in ACE2 humanized mice. MiR-486-MSC-Exo exerted anti-fibrotic effects through targeted inhibition of SMAD2 and activation of Akt phosphorylation. This study provides a potential therapeu approach for intervention RIPF.

Supplementary Information

The online version contains supplementary material available at https://doi.org/10.1186/s12951-024-02830-9.

Supplementary Material 1. Figure S1. Identification of CD90, CD73, CD105, CD45, CD34, and CD14 expression on the surface of control MSC using flow cytometry. Blue and red peaks represent MSC and Blank samples, respectively

Supplementary Material 2. Figure S2. mRNA expressionof A GPX4, B ACSL4, and C SLC7A11 in MLE-12 cells treated with MSC-Exo or miR-486-MSC-Exo after irradiationusing qPCR. Fer-1 was used as a positive control. Data are expressed as the mean±SD. *$p < 0.05$, **$p < 0.01$.

Supplementary Material 3. Figure S3. Fluorescent quantitation in confocal images of A dihydroethidiumand B mitochondriaof MLE-12 cells treated with MSC-Exo or miR-486-MSC-Exo after adding erastin. Fer-1 was used as a positive control. n=4，Data are expressed as the mean ± SD. *$p < 0.05$, **$p < 0.01$.

Acknowledgements

Not applicable.

Author contributions

Conceptualization, Feng-Jun Xiao and Li-Sheng Wang; Methodology and investigation, Ting-Ting Liu, Yi-Zhu Chen and Hui-Yan Sun; Resources and data Curation, Li Du, Yang Sun, Xiao-Chen Cheng and Yu-Xin Lu; Original Draft Preparation, review and editing, Wei-Yuan Zhang and Li Wen; Funding Acquisition, Feng-Jun Xiao and Li-Sheng Wang. All authors read and approved the final manuscript.

Funding

This work was supported by National Natural Science Foundation of China (Grant No. 82073489), Natural Science Foundation of Shandong Province (Grant No. ZR2020MH327, ZR2023ZD49), Natural Science Foundation of Hebei Province (Grant No.H2024103005) and Science and Technology Enhancement Program of Hebei Province (Grant No. 22567663H).

Availability of data and materials

No datasets were generated or analysed during the current study.

Declarations

Ethics approval and consent to participate

Not applicable.

Consent for publication
Not applicable.

Competing interests
The authors declare no competing interests.

Author details
[1]Department of Special Medicine, School of Basic Medicine, Qingdao University, Qingdao 266071, People's Republic of China. [2]Laboratory of Molecular Diagnosis and Regenerative Medicine, The Affiliated Hospital of Qingdao University, Qingdao 266000, People's Republic of China. [3]School of Nursing, Jilin University, Changchun 130021, Jilin, People's Republic of China. [4]Beijing Institute of Radiation Medicine, Beijing 100850, People's Republic of China. [5]Department of Pulmonary and Critical Care Medicine, The Second Medical Center, National Clinical Research Center for Geriatric Diseases, Chinese PLA General Hospital, Beijing 100853, China. [6]Yanda Medical Research Institute, Hebei Yanda Hospital, Langfang 065201, China.

Received: 9 May 2024 Accepted: 2 September 2024
Published online: 26 October 2024

References

1. Hanania AN, Mainwaring W, Ghebre YT, Hanania NA, Ludwig M. Radiation-induced lung injury: assessment and management. Chest. 2019;156:150–62.
2. Yan Y, Fu J, Kowalchuk RO, Wright CM, Zhang R, Li X, Xu Y. Exploration of radiation-induced lung injury, from mechanism to treatment: a narrative review. Transl Lung Cancer Res. 2022;11:307–22.
3. Kim N, Cho SG. Clinical applications of mesenchymal stem cells. Korean J Intern Med. 2013;28:387–402.
4. Zanoni M, Cortesi M, Zamagni A, Tesei A. The role of mesenchymal stem cells in radiation-induced lung fibrosis. Int J Mol Sci. 2019;20(16):3876.
5. Xu R, Feng Z, Wang FS. Mesenchymal stem cell treatment for COVID-19. EBioMedicine. 2022;77: 103920.
6. Lei J, Jiang X, Li W, Ren J, Wang D, Ji Z, Wu Z, Cheng F, Cai Y, Yu ZR, et al. Exosomes from antler stem cells alleviate mesenchymal stem cell senescence and osteoarthritis. Protein Cell. 2022;13:220–6.
7. Wang S, Lei B, Zhang E, Gong P, Gu J, He L, Han L, Yuan Z. Targeted therapy for inflammatory diseases with mesenchymal stem cells and their derived exosomes: from basic to clinics. Int J Nanomedicine. 2022;17:1757–81.
8. Ruonan X, Zhiqian F, Fu-Sheng W: Mesenchymal stem cell treatment for COVID-19. *EBioMedicine* 2022, 77.
9. Ruenn Chai L, Ronne Wee Yeh Y, Sai Kiang L: Mesenchymal stem cell exosomes. *Semin Cell Dev Biol* 2015, 40.
10. Phan J, Kumar P, Hao D, Gao K, Farmer D, Wang A. Engineering mesenchymal stem cells to improve their exosome efficacy and yield for cell-free therapy. J Extracell Vesicles. 2018;7:1522236.
11. Lou G, Chen L, Xia C, Wang W, Qi J, Li A, Zhao L, Chen Z, Zheng M, Liu Y. MiR-199a-modified exosomes from adipose tissue-derived mesenchymal stem cells improve hepatocellular carcinoma chemosensitivity through mTOR pathway. J Exp Clin Cancer Res. 2020;39:1–9.
12. Jiang L, Driedonks TAP, Jong WSP, Dhakal S, van den Berg B, van Saparoea H, Sitaras I, Zhou R, Caputo C, Littlefield K, Lowman M, et al. A bacterial extracellular vesicle-based intranasal vaccine against SARS-CoV-2 protects against disease and elicits neutralizing antibodies to wild-type and Delta variants. J Extracell Vesicles. 2022;11:12192.
13. Popowski KD, Moatti A, Scull G, Silkstone D, Lutz H, de Juan L, Abad B, George A, Belcher E, Zhu D, Mei X, et al. Inhalable dry powder mRNA vaccines based on extracellular vesicles. Matter. 2022;5:2960–74.
14. Liu K, Pan X, Li L, Yu F, Zheng A, Du P, Han P, Meng Y, Zhang Y, Wu L, et al. Binding and molecular basis of the bat coronavirus RaTG13 virus to ACE2 in humans and other species. Cell. 2021;184(3438–3451): e3410.
15. Ortiz M, Thurman A, Pezzulo A, Leidinger M, Klesney-Tait J, Karp P, Tan P, Wohlford-Lenane C, McCray P, Meyerholz D. Heterogeneous expression of the SARS-Coronavirus-2 receptor ACE2 in the human respiratory tract. EBioMedicine. 2020;60: 102976.
16. Ziegler CG, Allon SJ, Nyquist SK, Mbano IM, Miao VN, Tzouanas CN, Cao Y, Yousif AS, Bals J, Hauser BM, Feldman J. SARS-CoV-2 receptor ACE2 is an interferon-stimulated gene in human airway epithelial cells and is detected in specific cell subsets across tissues. Cell. 2020;181(5):1016–35.
17. Yang S, Liu P, Jiang Y, Wang Z, Dai H, Wang C. Therapeutic applications of mesenchymal stem cells in idiopathic pulmonary fibrosis. Front Cell Dev Biol. 2021;9: 639657.
18. Fu H, Tie Y, Xu C, Zhang Z, Zhu J, Shi Y, Jiang H, Sun Z, Zheng X. Identification of human fetal liver miRNAs by a novel method. FEBS Lett. 2005;579:3849–54.
19. Wang LS, Li L, Li L, Chu S, Shiang KD, Li M, Sun HY, Xu J, Xiao FJ, Sun G, et al. MicroRNA-486 regulates normal erythropoiesis and enhances growth and modulates drug response in CML progenitors. Blood. 2015;125:1302–13.
20. Kim J, Lee C, Shin Y, Wang S, Han J, Kim M, Kim JM, Shin SC, Lee BJ, Kim TJ, Jung Y. sEVs from tonsil-derived mesenchymal stromal cells alleviate activation of hepatic stellate cells and liver fibrosis through miR-486-5p. Mol Therapy. 2021;29(4):1471–86.
21. Ji X, Wu B, Fan J, Han R, Luo C, Wang T, Yang J, Han L, Zhu B, Wei D, et al. The anti-fibrotic effects and mechanisms of MicroRNA-486-5p in pulmonary fibrosis. Sci Rep. 2015;5:14131.
22. Yan Z, Ao X, Liang X, Chen Z, Liu Y, Wang P, Wang D, Liu Z, Liu X, Zhu J, et al. Transcriptional inhibition of miR-486-3p by BCL6 upregulates Snail and induces epithelial-mesenchymal transition during radiation-induced pulmonary fibrosis. Respir Res. 2022;23:104.
23. Xu S, Liu C, Ji HL. Concise review: therapeutic potential of the mesenchymal stem cell derived secretome and extracellular vesicles for radiation-induced lung injury: progress and hypotheses. Stem Cells Transl Med. 2019;8:344–54.
24. Yuan ZH, Liu T, Wang H, Xue LX, Wang JJ. Fatty acids metabolism: the bridge between ferroptosis and ionizing radiation. Front Cell Dev Biol. 2021;9: 675617.
25. Huang X, Song Y, Wei L, Guo J, Xu W, Li M. The emerging roles of ferroptosis in organ fibrosis and its potential therapeutic effect. Int Immunopharmacol. 2023;116: 109812.
26. Ebrahimi N, Adelian S, Shakerian S, Afshinpour M, Chaleshtori SR, Rostami N, Rezaei-Tazangi F, Beiranvand S, Hamblin MR, Aref AR. Crosstalk between ferroptosis and the epithelial-mesenchymal transition: Implications for inflammation and cancer therapy. Cytokine Growth Factor Rev. 2022;64:33–45.
27. Pei Z, Qin Y, Fu X, Yang F, Huo F, Liang X, Wang S, Cui H, Lin P, Zhou G, et al. Inhibition of ferroptosis and iron accumulation alleviates pulmonary fibrosis in a bleomycin model. Redox Biol. 2022;57: 102509.
28. Fang L, Shi X, Sun H, Li Y, Xiao F, Wang H, Wang L. Effects of exosomes derived from miR-486 gene modified umbilical cord mesenchymal stem cells on biological characteristics of rat cardiomyocytes. Zhongguo Shi Yan Xue Ye Xue Za Zhi. 2018;26:1531–7.
29. Fu Y, Xiong S. Tagged extracellular vesicles with the RBD of the viral spike protein for delivery of antiviral agents against SARS-COV-2 infection. J Control Release. 2021;335:584–95.
30. Ying H, Fang M, Hang QQ, Chen Y, Qian X, Chen M. Pirfenidone modulates macrophage polarization and ameliorates radiation-induced lung fibrosis by inhibiting the TGF-beta1/Smad3 pathway. J Cell Mol Med. 2021;25:8662–75.
31. Zheng L, Zhu Q, Xu C, Li M, Li H, Yi PQ, Xu FF, Cao L, Chen JY. Glycyrrhizin mitigates radiation-induced acute lung injury by inhibiting the HMGB1/TLR4 signalling pathway. J Cell Mol Med. 2020;24:214–26.
32. Sun XH, Wang X, Zhang Y, Hui J. Exosomes of bone-marrow stromal cells inhibit cardiomyocyte apoptosis under ischemic and hypoxic conditions via miR-486-5p targeting the PTEN/PI3K/AKT signaling pathway. Thromb Res. 2019;177:23–32.
33. Lou G, Chen L, Xia C, Wang W, Qi J, Li A, Zhao L, Chen Z, Zheng M, Liu Y. MiR-199a-modified exosomes from adipose tissue-derived mesenchymal stem cells improve hepatocellular carcinoma chemosensitivity through mTOR pathway. J Exp Clin Cancer Res. 2020;39:4.
34. Li B, Li C, Zhu M, Zhang Y, Du J, Xu Y, Liu B, Gao F, Liu H, Cai J, Yang Y. Hypoxia-induced mesenchymal stromal cells exhibit an enhanced therapeutic effect on radiation-induced lung injury in mice due to an increased proliferation potential and enhanced antioxidant ability. Cell Physiol Biochem. 2017;44:1295–310.
35. Wang Z, Popowski KD, Zhu D, de Juan Abad BL, Wang X, Liu M, Lutz H, De Naeyer N, DeMarco CT, Denny TN, et al. Exosomes decorated with

a recombinant SARS-CoV-2 receptor-binding domain as an inhalable COVID-19 vaccine. Nat Biomed Eng. 2022;6:791–805.
36. Matsuzaka Y, Yashiro R. Therapeutic strategy of mesenchymal-stem-cell-derived extracellular vesicles as regenerative medicine. Int J Mol Sci. 2022;23(12):6480.
37. Ziegler CGK, Allon SJ, Nyquist SK, Mbano IM, Miao VN, Tzouanas CN, Cao Y, Yousif AS, Bals J, Hauser BM, et al. SARS-CoV-2 receptor ACE2 is an interferon-stimulated gene in human airway epithelial cells and is detected in specific cell subsets across tissues. Cell. 2020;181:1016-1035. e1019.
38. Shang J, Ye G, Shi K, Wan Y, Luo C, Aihara H, Geng Q, Auerbach A, Li F. Structural basis of receptor recognition by SARS-CoV-2. Nature. 2020;581:221–4.
39. Starr TN, Greaney AJ, Hilton SK, Ellis D, Crawford KHD, Dingens AS, Navarro MJ, Bowen JE, Tortorici MA, Walls AC, et al. Deep mutational scanning of SARS-CoV-2 receptor binding domain reveals constraints on folding and ACE2 binding. Cell. 2020;182(1295–1310): e1220.
40. El-Shennawy L, Hoffmann AD, Dashzeveg NK, McAndrews KM, Mehl PJ, Cornish D, Yu Z, Tokars VL, Nicolaescu V, Tomatsidou A, et al. Circulating ACE2-expressing extracellular vesicles block broad strains of SARS-CoV-2. Nat Commun. 2022;13:405.
41. Wang B, Wei J, Meng L, Wang H, Qu C, Chen X, Xin Y, Jiang X. Advances in pathogenic mechanisms and management of radiation-induced fibrosis. Biomed Pharmacother. 2020;121: 109560.
42. Huang Y, Zhang W, Yu F, Gao F. The cellular and molecular mechanism of radiation-induced lung injury. Med Sci Monit. 2017;23:3446–50.
43. Hade MD, Suire CN, Suo Z. Mesenchymal stem cell-derived exosomes: applications in regenerative medicine. Cells. 2021;10(8):1959.
44. Zhao T, Sun F, Liu J, Ding T, She J, Mao F, Xu W, Qian H, Yan Y. Emerging role of mesenchymal stem cell-derived exosomes in regenerative medicine. Curr Stem Cell Res Ther. 2019;14:482–94.
45. Kim SM, Jeong CH, Woo JS, Ryu CH, Lee JH, Jeun SS. In vivo near-infrared imaging for the tracking of systemically delivered mesenchymal stem cells: tropism for brain tumors and biodistribution. Int J Nanomedicine. 2016;11:13–23.
46. Lu CH, Chen YA, Ke CC, Chiu SJ, Chen CC, Hsieh YJ, Yang BH, Liu RS. Preclinical characterization and in vivo imaging of (111)in-labeled mesenchymal stem cell-derived extracellular vesicles. Mol Imaging Biol. 2021;23:361–71.
47. Tsai SJ, Atai NA, Cacciottolo M, Nice J, Salehi A, Guo C, Sedgwick A, Kanagavelu S, Gould SJ. Exosome-mediated mRNA delivery in vivo is safe and can be used to induce SARS-CoV-2 immunity. J Biol Chem. 2021;297(5):101266.
48. Foo JB, Looi QH, How CW, Lee SH, Al-Masawa ME, Chong PP, Law JX. Mesenchymal stem cell-derived exosomes and microrna in cartilage regeneration: biogenesis, efficacy, mirna enrichment and delivery. Pharmaceuticals. 2021;14(11):1093.
49. Li R, Jia Y, Kong X, Nie Y, Deng Y, Liu Y. Novel drug delivery systems and disease models for pulmonary fibrosis. J Controlled Release. 2022;348:95–114.
50. Navon R, Wang H, Steinfeld I, Tsalenko A, Ben-Dor A, Yakhini Z. Novel rank-based statistical methods reveal microRNAs with differential expression in multiple cancer types. PLoS ONE. 2009;4: e8003.
51. Douvris A, Vinas J, Burns KD. miRNA-486-5p: signaling targets and role in non-malignant disease. Cell Mol Life Sci. 2022;79:376.
52. Wei W, Liu C, Yao R, Tan Q, Wang Q, Tian H. MiR-486-5p suppresses gastric cancer cell growth and migration through downregulation of fibroblast growth factor 9. Mol Med Rep. 2021;24(5):1.
53. Yen TA, Huang HC, Wu ET, Chou HW, Chou HC, Chen CY, Huang SC, Chen YS, Lu F, Wu MH, Tsao PN. Microrna-486-5P regulates human pulmonary artery smooth muscle cell migration via endothelin-1. Int J Mol Sci. 2022;23(18):10400.
54. Deleon N, Adem S, Lavin C, Abbas D, Griffin M, King M, Borrelli M, Patel R, Fahy E, Lee D, et al. Angiogenic CD34+CD146+ adipose-derived stromal cells augment recovery of soft tissue after radiotherapy. J Tissue Eng Regen Med. 2021;15:1105–17.
55. Jin J, Shi Y, Gong J, Zhao L, Li Y, He Q, Huang H. Exosome secreted from adipose-derived stem cells attenuates diabetic nephropathy by promoting autophagy flux and inhibiting apoptosis in podocyte. Stem Cell Res Ther. 2019;10:95.
56. Xiao Y. viaMiR-486-5p inhibits the hyperproliferation and production of collagen in hypertrophic scar fibroblasts IGF1/PI3K/AKT pathway. J Dermatolog Treat. 2021;32:973–82.
57. Xu L, Zhang Y, Long H, Zhou B, Jiang H. βmiR-486-5p restrains extracellular matrix production and oxidative damage in human trabecular meshwork cells by targeting TGF-/SMAD2 pathway. J Ophthalmol. 2022;2022:3584192.
58. Viñas JL, Spence M, Porter CJ, Douvris A, Gutsol A, Zimpelmann JA, Campbell PA, Burns KD. micro-RNA-486-5p protects against kidney ischemic injury and modifies the apoptotic transcriptome in proximal tubules. Kidney Int. 2021;100:597–612.
59. Zhang Y, Tan H, Daniels JD, Zandkarimi F, Liu H, Brown LM, Uchida K, O'Connor OA, Stockwell BR. Imidazole ketone erastin induces ferroptosis and slows tumor growth in a mouse lymphoma model. Cell Chem Biol. 2019;26(5):623–33.
60. Xiao FJ, Zhang D, Wu Y, Jia QH, Zhang L, Li YX, Yang YF, Wang H, Wu CT, Wang LS. miRNA-17-92 protects endothelial cells from erastin-induced ferroptosis through targeting the A20-ACSL4 axis. Biochem Biophys Res Commun. 2019;515:448–54.
61. Lin F, Chen W, Zhou J, Zhu J, Yao Q, Feng B, Feng X, Shi X, Pan Q, Yu J, et al. Mesenchymal stem cells protect against ferroptosis via exosome-mediated stabilization of SLC7A11 in acute liver injury. Cell Death Dis. 2022;13:271.
62. Li X, Duan L, Yuan S, Zhuang X, Qiao T, He J. Ferroptosis inhibitor alleviates Radiation-induced lung fibrosis (RILF) via down-regulation of TGF-β1. J Inflamm (Lond). 2019;16:11.
63. Aleksandr K, Ashley Rose R, David N, Daniel C, Heather M-M, Robert Matthew K: Association between weight loss and mortality in idiopathic pulmonary fibrosis. *Respir Res* 2022,23.
64. Douvris A, Viñas J, Burns KD. miRNA-486-5p: signaling targets and role in non-malignant disease. Cell Mol Life Sci. 2022;79(7):376.
65. Chen S, Li K, Zhong X, Wang G, Wang X, Cheng M, Chen J, Chen Z, Chen J, Zhang C, Xiong G. Sox9-expressing cells promote regeneration after radiation-induced lung injury via the PI3K/AKT pathway. Stem Cell Res Therapy. 2021;12(1):381.
66. Viñas J, Burger D, Zimpelmann J, Haneef R, Knoll W, Campbell P, Gutsol A, Carter A, Allan D, Burns K. Transfer of microRNA-486-5p from human endothelial colony forming cell-derived exosomes reduces ischemic kidney injury. Kidney Int. 2016;90:1238–50.
67. Viñas J, Spence M, Gutsol A, Knoll W, Burger D, Zimpelmann J, Allan D, Burns K. Receptor-ligand interaction mediates targeting of endothelial colony forming cell-derived exosomes to the kidney after ischemic injury. Sci Rep. 2018;8:16320.

Publisher's Note